Precipitation Regimes in Haiti: A Clustering Analysis Using Chirpsv2 Data (Period 1981-2020)

Didier Bernard, Romual Chery, Emmanuel Biabiany, Raphaël Cécé

▶ **To cite this version:**

Didier Bernard, Romual Chery, Emmanuel Biabiany, Raphaël Cécé. Precipitation Regimes in Haiti: A Clustering Analysis Using Chirpsv2 Data (Period 1981-2020). 2025. ⟨hal-05360857⟩

HAL Id: hal-05360857

https://univ-antilles.hal.science/hal-05360857v1

Preprint submitted on 12 Nov 2025

HAL is a multi-disciplinary open access archive for the deposit and dissemination of scientific research documents, whether they are published or not. The documents may come from teaching and research institutions in France or abroad, or from public or private research centers.

L'archive ouverte pluridisciplinaire **HAL**, est destinée au dépôt et à la diffusion de documents scientifiques de niveau recherche, publiés ou non, émanant des établissements d'enseignement et de recherche français ou étrangers, des laboratoires publics ou privés.

HAL Authorization

Precipitation Regimes in Haiti: A Clustering Analysis using CHIRPSv2 Data (Period 1981-2020)

Didier C. Bernard[a*], Romual Chery[a], Emmanuel Biabiany[b], and Raphaël Cécé[a]

Affiliations:

a LARGE, University of the French West Indies, 97157 Pointe-à-Pitre, Guadeloupe, France

b LAMIA, University of the French West Indies, 97157 Pointe-à-Pitre, Guadeloupe, France

[*]**Corresponding author:**

didier.bernard@univ-antilles.fr,

Preprint not peer reviewed

This preprint research paper has not been peer reviewed. Electronic copy available at: https://ssrn.com/abstract=5243924

Abstract. This study aims to determine rainfall trends in Haiti from 1981 to 2020 using the Climate Hazards Group InfraRed Precipitation with Station data 2.0 (CHIRPSv2) dataset. Because of the scarcity of rain gauge stations in this complex topographical region, this gridded dataset was selected to compensate for the data deficit and provide an updated analysis of the country's spatiotemporal precipitation variability. Based on Kullback-Leibler divergence and cluster analysis, Haiti can be classified into four distinct zones with seven precipitation regimes (three wet, three dry, and one transitional). Wet regimes dominate the early and late rainy seasons, whereas dry regimes prevail throughout the dry season (December to March). The intermediate regime is associated with the regression of the mid-summer drought. Rainfall years are characterized by four to seven regimes that affect inter-annual and intra-annual precipitation variability. Drought periods and major climate influences are present, including the El Niño-Southern Oscillation and North Atlantic Oscillation. Climate anomalies and composites caused by fluctuations in sea surface temperature and upper-level wind patterns contribute to the transition between dry and wet regimes. This study concludes that CHIRPSv2 data provide reliable estimates for assessing precipitation trends, facilitating water resource management, and climate change adaptation. However, some limitations remain, particularly the underestimation of precipitation in mountainous locations, emphasizing the need for further research to improve local coverage.

Keywords

CHIRPSv2, Haiti, Kullback–Leibler divergence, Expert Distance, KGE , Precipitation regimes.

Highlights:

- Four spatially coherent rainfall zones were found in Haiti
- Seven spatio-temporal rainfall distributions were identified using CHIRPSv2 data
- Estimated transition probabilities show high variability in annual sequences
- Abnormally dry or wet years cannot be linked to specific intra-annual scenarios
- Large-scale climate factors could not be linked to precipitation variability

Preprint not peer reviewed

This preprint research paper has not been peer reviewed. Electronic copy available at: https://ssrn.com/abstract=5243924

1. Introduction

Precipitation, monitored on a daily to annual basis, is crucial to the most engaging studies in the Caribbean, such as climate change impact assessments, water resource management, and hydrological modeling.

On the leeward side of the island of Hispaniola, Haiti experiences highly heterogeneous rainfall patterns due to its rugged terrain, intricate coastline, and the influence of surrounding warm waters. Rainfall not only replenishes freshwater resources but also sustains healthy ecosystems—such as forests, rivers, and wetlands—that offer crucial services like erosion control and biodiversity conservation. As an agrarian country, Haiti depends heavily on seasonal rains to sustain its crops. However, its steep terrain makes it particularly vulnerable to the damaging effects of extreme rainfall, such as flash floods and landslides, as ENSO-related climate variability is likely to increases the irregularity and intensity of these events. These hazards can destroy infrastructure, promote epidemics, displace communities, and cause loss of life, particularly in densely populated or deforested regions (FAO, 2024). Irregular or insufficient rainfall can lead to prolonged droughts (Elusma et al., 2022), reducing agricultural yields and exacerbating water scarcity (Singh and Barton-Dock, 2015). Given the country's vulnerability to climate change, understanding annual variability and rainfall patterns are increasingly critical for early warning systems and disaster preparedness (Eisenberg et al., 2013).

The general patterns of the dry and wet seasons in Haiti closely align with those observed across the broader Antillean region (Alpert, 1942). Rainy season coincides with the seasonal northward migration of the Intertropical Convergence Zone and the North Atlantic Anticyclone (Gu and Adler, 2006; Gamble and Curtis, 2008; Angeles et al., 2010), the weakening of trade winds and the Caribbean Low-Level Jet (CLLJ), and the warming of the western hemisphere warm pool (Wang et al., 2007; Moron et al., 2016). The observed annual precipitation cycle has a bimodal annual distribution, with the rainy season divided into an early rainy season (ERS) from April to May and a late rainy season (LRS) from August to November (Chen and Taylor, 2002). The mid-summer drought (MSD), a relative decrease in precipitation centered around July,

Preprint not peer reviewed

This preprint research paper has not been peer reviewed. Electronic copy available at: https://ssrn.com/abstract=5243924

separates these two peaks (Magaña et al. 1999; Curtis and Gamble, 2008; Gamble and Curtis, 2008). The winter dry season (WDS) lasts from December to March.

Studies have also examined how teleconnections such as the El Niño-Southern Oscillation (ENSO) and North Atlantic Oscillation (NAO) affect the regional mechanisms of interannual precipitation variability in the Caribbean. These studies are built on composites of ocean-atmosphere anomalies derived from reanalysis of surface level pressure (SLP) and sea surface temperature (SST) during various phases of ENSO and NAO. These two oscillations have also been shown to affect SST anomalies in the North Tropical Atlantic, which modulate the amount of precipitation in the region (Enfield and Alfaro, 1999; Giannini et al., 2001; Chen and Taylor, 2002; Jury et al., 2007; Taylor et al., 2011; Gouirand et al., 2012, 2014). During warm ENSO years, the Caribbean region typically experiences summer conditions that are drier than normal (year 0). The dry conditions are caused by a shift in deep convection to the eastern Pacific, resulting in surface divergence in the Caribbean. These incidents cause wetter conditions in the spring of the following year (year +1), which are linked to the delayed warming of the North Tropical Atlantic. The rains in March-April-May are triggered and exacerbated by more frequent incursions of westward troughs in the subtropical jet into the Caribbean during ENSO, which cause convective heating and evaporation due to SST anomalies (> 26 °C) and altered large-scale wind flow (Laing, 2004; Jury, 2023).

The positive phases of the NAO (high pressure over the North Subtropical Atlantic) are associated with reduced precipitation in the Caribbean. This reduction is ascribed to increased atmospheric subsidence along with negative SST anomalies caused by stronger trade winds. The NAO has an impact independent of ENSO. However, combined NAO-ENSO effects, such as a positive NAO phase and a warm ENSO event, resulted in exceptionally dry conditions that summer (year 0). Jury et al. (2007) confirmed the impact of warm ENSO episodes and found that the correlation between the NAO signal and precipitation remained less significant. Using monthly totals from 35 ground stations collected between 1951 and 1998, they identified four groups of bimodal precipitation with distinct seasonal patterns. The rain gauges were placed throughout the Caribbean Arch, from northwest to southeast (Jury et al., 2007).

Jury and Gouirand (2011) used SST and SLP composites to identify pronounced decadal oscillations (9-11 years), which were more significant in the northern islands than in the southeast. They highlighted the intensified activity of the Atlantic

Preprint not peer reviewed

This preprint research paper has not been peer reviewed. Electronic copy available at: https://ssrn.com/abstract=5243924

Intertropical Convergence Zone (ITCZ), which is associated with SLP and SST during specific phases of the decadal mode. To better understand Caribbean precipitation variability, additional atmospheric and oceanic predictors of low-frequency climate modulation were investigated. Moron et al. (2016) used daily Outgoing Longwave Radiation (OLR) and 925 hPa wind circulation to delineate eight weather types (WT). The three wet weather types manifest from May to October, corresponding with increasing deep convection, whereas the five dry types appear from November to April and are associated with large-scale subsidence.

Over the last decade, published research has focused on developing models of intraseasonal behavior based on moisture balance and precipitable water in the atmospheric column. Allen and Mapes (2017) defined a new climatological tropical rainfall belt based on satellite-derived total precipitable water (TPW) in the atmosphere (Morphed Integrated Microwave Imagery at CIMSS–MIMIC). This belt extends across the Greater Antilles along a diagonal from 13° N to 24° N, from the southwestern Caribbean to the Bahamas. Rainfall in this region is largely determined by Lagrangian statistics relating to the influx of moist air brought from the equatorial latitudes by low-level southerly winds. Seasonal warming causes this belt to strengthen, and moisture availability coincides with the onset of the ERS in mid-May.

Martinez et al. (2019, 2020) demonstrated that the seasonal cycle of precipitation in the Caribbean is determined by three large-scale climate drivers of moisture convergence: the Eastern Pacific ITCZ, the Atlantic ITCZ, and the western flank of the North Atlantic Subtropical High (NASH). The spatial distribution of moisture is driven by the CLLJ and the Atlantic warm pool. The expansion or contraction of the western flank of the NASH modulates the bimodal annual rainfall pattern in the northwestern and central Caribbean and, in association with the Eastern Pacific ITCZ, influences the western Caribbean. They identified the Atlantic ITCZ as the principal source of precipitation for the central and southern Lesser Antilles. A positive NAO causes drier years during the ERS due to wind-evaporation-SST feedback, which manifests as stronger trade winds overcoming a persistent SST dipole between the Caribbean Sea and the Gulf of Mexico. The inter-basin SLP model, which removes moisture from the Caribbean at the onset of summer during El Niño events, results in drier LRS years. The authors stated that the NAO and ENSO had opposing effects during their respective phases -resulting in wet years in both seasons- and

Preprint not peer reviewed

This preprint research paper has not been peer reviewed. Electronic copy available at: https://ssrn.com/abstract=5243924

concluded that the two rainy seasons were independent as their primary drivers of variability differ.

Gouirand et al. (2020, 2024) studied the winter-to-summer (W2S) and summer-to-winter (S2W) transitions, as well as the detection and functioning of Moisture Sink Days (MSDy) based on the previously mentioned weather types. In the first case, they found a sharp W2S transition characterized by increased precipitation and weakening of the CLLJ, but no significant SST anomalies. The S2W transition appears to be driven by changes in SST anomalies in the Caribbean, with interannual variations showing relative independence in the interannual from those of W2S transitions. Using weather types rather than local precipitation data, these authors established that the observed MSD from mid-June to mid-August was caused by a cessation of the North Atlantic Subtropical High's eastward progress, not a predicted westward shift. They found no significant correlation between the onset of MSDy-WT and SST in the tropical North Atlantic or Eastern Tropical Pacific. The monsoon circulation over Mesoamerica is thought to be a prelude for increased subsidence over the Caribbean basin, synchronized acceleration of the CLLJ, and amplified deep convection in Central America and Mexico.

Collectively, these studies provide valuable insights into the primary drivers and climatic mechanisms that influence intra- and interannual precipitation variability at large and medium scales in the Antillean. Most publications on this topic have relied primarily on observations from ground-based rain gauge networks, with limited use of gridded precipitation products offering broader spatial and temporal coverage.

It has been noted that these studies frequently fail to account smaller-scale variability, as incomplete ground-based data coverage across island territories. As a result, there is a risk of failing to account for the full spatiotemporal variability of precipitation in these regions, particularly because they include both arid coastal zones and steep mountain ranges. Studying the precipitation variability in a specific territory is crucial for developing diagnostics for water resource management (food security, agriculture, and urban planning), natural risk prevention (floods and droughts), and climate change adaptation. Further research is needed in regions with scarce rain gauge networks.

In this study, we focused on Haiti, which is characterized by a conventional rain-gauge network that has decreased in density and frequency of observations (Moron

Preprint not peer reviewed

This preprint research paper has not been peer reviewed. Electronic copy available at: https://ssrn.com/abstract=5243924

et al., 2015). Although Bathélémy et al. (2024) recently offered the scientific community an open-access database called Simbi (last access date: https://doi.org/10.23708/02POK6), this terrain remains a grey area because of the difficulties in obtaining recent and accurate rain gauge data. The availability of high-quality observational precipitation data with extensive spatiotemporal coverage is a major challenge. This study proposes using gridded data (0.05° x 0.05°) from the Climate Hazards Group InfraRed Precipitation with Station data V2 (CHIRPS; Funk et al., 2015) to identify potential precipitation regimes and analyze and update intra- and interannual precipitation trends in Haiti. Its tropical, insular, and orographic environments make this territory an excellent case study for validating CHIRPS data and assessing its capacity to capture regional precipitation variability. The use of gridded data, combined with novel identification methods based on Kullback-Leibler divergence, can provide a new perspective for updating trends and potentially providing more complete behavioral models. Overall, rainfall in Haiti is both a lifeline and a risk factor, making its monitoring and analysis essential for sustainable development and resilience planning.

The remaining sections of this paper are organized as follows. Section 2 describes the dataset, and the procedures employed. Section 3 focuses on the spatial composites of climate factors that contribute to the interannual variability of the rainfall cycle in Haiti. The homogeneity of the interannual rainfall variability was also investigated. Finally, section 4 concludes the study.

2. Methods and Materials

2.1 Study region

Haiti is situated on the island of Hispaniola in the northeastern Caribbean, between 71°42′ and 74°29′ W longitude and 18°00′ and 20°07′ N latitude.

Haiti covers 27,750 km^2 and has a population of 12 million (https://ihsi.gouv.html; accessed February 14, 2025).

Fig. 1 depicts a country with a complex topography that includes steep mountains, valleys, and coastal plains, with a physiognomy varying from east to west and north to south.

Preprint not peer reviewed

This preprint research paper has not been peer reviewed. Electronic copy available at: https://ssrn.com/abstract=5243924

2.2 Rain gauge data

This study relied on a monthly rain gauge network dataset from a hydrometeorological unit. Monthly rainfall data were analyzed to determine the seasonal and interannual variability of rainfall.

The study ran from January 1961 to December 2018. However, many rain gauges record data for only one or three years. The databases were verified for duplicate rainfall measurements, missing data, and outliers. Between 1981 and 2018, only nine stations were selected, with less than 5% of them having outliers or missing values.

2.3 Satellite derived and reanalysis gridded rainfall data

To overcome the scarcity of current precipitation data, gridded monthly precipitation data from three global databases were examined. The Climate Hazards InfraRed Precipitation with Station data 2.0 (CHIRPSv2), Multi/Source Weighted/Ensemble Precipitation (MSWEP, Beck et al., 2017), and European Center of Medium-Range Weather Forecasts (ECMWF) Reanalysis v.5 (ERA5) were used. The CHIRPS product combines satellite Cold Cloud Duration (CCD) measurements calibrated using Tropical Rainfall Measuring Mission (TRMM) 3B42 data and rain-gauge station data (Funck et al., 2015). The first pentad database, the CHIRP, was developed. It was created using global precipitation archives from GridSat (Globally Gridded Satellite) and Climate Hazard Precipitation (CHPclim) that were then combined with estimated and calibrated CCD data. The pentadal CHIRP values were aggregated to monthly precipitation and scaled to a resolution of 0.05 degrees. The final CHIRPS product was a combination of the unadjusted and bias/adjusted CHIRP data from ground rain gauge stations. After reviewing a list of selected stations (available at https://data.chc.ucsb.edu/products/CHIRPS/2.0/diagnostics/list_of_stations_used/), we found that only two rain gauges were used for a single year (2020). Gridded monthly precipitation data from the 10-km global product Multi/Source Weighted/Ensemble Precipitation (MSWEP) (http://www.gloh2o.org/, September 28, 2024) were also investigated. The European Centre for Medium/Range Weather Forecasts (ECMWF) most recent fifth-generation reanalysis products, ERA5, were also used to examine gridded monthly total precipitation and sea surface temperature (ERA5 monthly averaged data on single levels from 1940 to present, July 04, 2024), as well as

Preprint not peer reviewed

This preprint research paper has not been peer reviewed. Electronic copy available at: https://ssrn.com/abstract=5243924

geopotential, U and V component of wind (ERA5 monthly averaged data on pressure levels from 1940 to present, July 04, 2024).

2.4 Methodology

2.4.1 Spatial comparison between gridded rainfall data and rain gauge data

Before evaluating and preparing the data for the classification algorithms, we ensured that the monthly precipitation data from the three global databases corresponded to the observed rain gauges. We compared the spatial patterns generated from the first empirical orthogonal function (EOF) of monthly rainfall data recorded by 62 rain gauge stations with those from the CHIRPSv2, MSWEP, and ERA5 databases for the period 1981-1990. The grid points used for the gridded databases were those closest to the ground stations (Fig. 2). The similarities between these spatial configurations were determined by comparing the EOF coefficients to each global base.

Categorical indices were used to compare monthly precipitation totals from different gridded products with the monthly data recorded by ground stations, which covered a large portion of the country yet had 10% missing values. The comparison indices used were the Root Mean Square Error (RMSE), bias, and Kling-Gupta Efficiency (KGE) (Gupta et al., 2009; Zambrano-Bigiarini et al., 2017). The KGE breaks down performance into three equally weighted components: linear correlation (r), bias ratio (β), and variability ratio (γ). The mean β values show whether the global products tend to overestimate ($\beta > 1$) or underestimate ($\beta < 1$) the observed values. The γ values provide information on the dispersion of these estimates.

To supplement this validation, wavelet transform analysis and the Morlet wavelet function were used to identify the periodicities in the oscillatory components of the CHIRPSv2 time series when compared to the rain gauge station time series (Torrence and Compo, 1998; Roesch and Schmidbauer, 2018).

2.4.2 Clustering analysis

The identification and clustering of spatiotemporal configurations describing the behavior of a physical parameter over a specific field requires a global approach that accounts for all characteristics of the examined field. Some configurations have weak patterns, necessitating the use of indicators that are highly sensitive to small distortions. To meet these requirements, we proposed the following approach: The study domain

Preprint not peer reviewed

This preprint research paper has not been peer reviewed. Electronic copy available at: https://ssrn.com/abstract=5243924

was initially spatially divided into significant regions using Principal Component Analysis (PCA), followed by a hierarchical ascending classification (HAC). The Euclidean distance was chosen as the metric for geographically clustering similar precipitation grid points, and Ward's criterion was employed for aggregation. The dataset used was the 12-month Standardized Precipitation Index (SPI12), a robust tool for quantifying precipitation deficits/excesses over several timescales (McKee, 1995). Its outstanding spatial coherence enables comparisons between geographic regions with distinct climatic conditions.

The symmetrized Kullback-Leibler divergence (DKLS) was used to assess variability in the studied physical field (Kullback and Leibler, 1951). This metric estimates the dissimilarity between two probability distributions of monthly precipitation totals by region while remaining sensitive to single fluctuations buried within the signal. Let $x_{1,s}$ and $x_{2,s}$ be two distributions of CHIRPSv2 monthly precipitation totals, which are real scalar stochastic processes acquired from two separate months within the same spatial region s. To examine the differences between these two processes, they were represented as discrete distributions (i.e., histograms) with bin boundaries determined by the deciles shown in Table 1.

The Kullback–Leibler divergence (DKL) was calculated using the following equation:

$$D_{KL}(x_{1,s},x_{2,s}) = p(x_{1,s})log\left(\frac{p(x_{1,s})}{p(x_{2,s})}\right) (1),$$

The DKL can be used to measure the dissimilarity of two distributions; however, it is not a distance function because it is not symmetrical. To offer a quantitative basis for the comparison, the pseudo-distance was calculated as follows:

$$D_{KLS}(x_{1,s},x_{2,s}) = D_{KL}(x_{1,s},x_{2,s}) + D_{KL}(x_{2,s},x_{1,s}). (2)$$

The ultimate comparison indicator, the Expert Distance (ED), is calculated using an averaging method using the following formula:

$$ED(x_1,x_2) = \frac{1}{n}\sum_{s=1}^{n} D_{KLS}(x_{1,s},x_{2,s}) (3)$$

where $x_1$and x_2 are two specified months, and n is the number of spatial zones determined by the HAC.

Preprint not peer reviewed

This preprint research paper has not been peer reviewed. Electronic copy available at: https://ssrn.com/abstract=5243924

The qualifier "expert" was used because the calculated value considers the spatial specificities of the geographical area analyzed by integrating the temporal dynamics of the physical parameter, in this instance precipitation (Biabiany et al., 2020; Bernard et al., 2022). We used an advanced version of the K-means algorithm, referred to as K-medoids (KMED-ED), to cluster these abstract groups of ED (Kaufman and Rousseeuw, 1990). This is an unsupervised method for addressing outlier data sensitivity.

The Silhouette Index was used to calculate the number of groups (or clusters) to be retained after performing various clustering techniques (Rousseeuw, 1987). This index also evaluates clustering quality by comparing intra-cluster homogeneity to inter-cluster heterogeneity. Figure 3 schematically outlines the complete methodology; no deseasonalization or seasonal conditioning steps were used to highlight the targeted structures. We did not study the anomalies because the goal of this study is to characterize the precipitation dynamics of each region.

2.4.3 Composites

To further understand the potential forcing associated with these clusters, seasonal anomalies and composites of geopotential, wind at 925 hPa isobars, atmospheric column total precipitation (TP), and SST were generated from monthly ERA5 reanalysis. The TP is the accumulated liquid and frozen water that falls on the Earth's surface, including rain and snow. This is the sum of large-scale precipitation and convective precipitation. The ECMWF Integrated Forecast System's cloud scheme generated large-scale precipitation, which was represented by uniform grids with a resolution of 0.25° (~31 km) (Hersbach et al., 2020). Anomalies and climatology (period 1981 to 2020) were calculated for the ranges of 100° W-50° W and 5° N-30° N.

SST data were chosen as the parameters driving marine convection and cloud production. The *u* and *v* components of the wind at 925 hPa were selected to include cloud transport and, more broadly, the moisture of the atmospheric base layers in the automatic analysis.

Anomalies and composites were generated by averaging the differences between each cluster's elements and the mean field for a given physical parameter as follows:

$$A_c = \frac{1}{N}\sum_{i=1}^{N}(x_i - \underline{x})$$

This preprint research paper has not been peer reviewed. Electronic copy available at: https://ssrn.com/abstract=5243924

where Ac is the mean anomaly, N is the number of elements, and x_i represents element *i* of cluster *c*. This procedure was performed using the geopotential at 925 hPa, SST, and precipitation data.

2.4.4 Statistical Analyses

Mean, standard deviation, interquartile range, coefficient of variation (CV), were used to allow relative comparison of data. The Wilcoxon signed rank test was used for ground data station comparisons. To assess whether the distribution of rainfall pattern characteristics in Haiti differs according to ENSO conditions, we used the chi-squared test. Python was used to calculate ED and to perform the clustering. All analyses were performed using R Statistical Software (v4.3.2; R Core Team 2021).

3. Results

3.1 Climatology of Precipitation from Different Databases

3.1.1 Ground Stations

Figure 4 depicts the annual rainfall distribution based on average monthly totals measured at six ground stations in Haiti for the period from 1961 to 2018. The annual totals at these stations ranged between 728 and 2837 mm, with an average of 1250–1690 mm (Table 2). The patterns seen in this figure are comparable to those observed in the Caribbean (Jury et al., 2007). The dry season was clearly defined as December to March, whereas two maxima often occurred in May and September-October, corresponding to the ERS and LRS, respectively (Fig. 4). Wilcoxon comparison tests found significant differences ($P = 0.03$) in the annual accumulations measured in the southern and northern regions (not shown). Coefficients of variation ranging from 15 to 28% suggested the presence of intra- and inter-annual variability.

3.1.2 Comparative Performance Evaluation of Gridded Databases (CHIRPSv2, MSWEP, and ERA5)

Empirical orthogonal functions (EOFs) were used to identify the most prominent spatial patterns in gridded data from CHIRPSv2, MSWEP, and ERA5. These patterns were compared to those acquired from ground stations from 1981 to 1990, using only grid points nearest to the ground stations (Fig. 2).

The first EOF mode (EOF1), weighted by the maximum ($0.4 < \text{ratio} < 1$), identifies shared spatial features between the three gridded databases and the ground station data

Preprint not peer reviewed

This preprint research paper has not been peer reviewed. Electronic copy available at: https://ssrn.com/abstract=5243924

(Fig. 4). The EOF1 variances were 43% for the ground stations, 72% for CHIRPSv2, 81.1% for ERA5, and 83.3% for MSWEP. The spatial distributions of EOF1 in CHIRPSv2 and the ground observations were very similar (Fig. 4). The western tip of the northern peninsula and a portion of the Artibonite coastal area remain the driest regions. The rainiest areas were found on the southern peninsula, centered around the Massif de la Hotte, and in central Haiti, surrounding the Montagne Noire. The EOF1 of the MSWEP data differs from the preceding two (ground stations and CHIRPSv2) in that it displays a less selective spatial distribution of rainfall totals for Haiti. The ERA5 dataset showed the most discordant pattern, deviating from reality, as the areas with the highest rainfall totals (ratio > 0.7) were in the western department (around Port-au-Prince) and sections of Artibonite (identified as dry zones by other databases and ground observations).

Spatial examination of the selected stations showed that the periods better replicated by CHIRPSv2 compared to the precipitation data corresponded to intra-annual variability for the bands of 0.5 and 1 year. Long-term patterns (more than one year) were not as well represented by CHIRPSv2 and showed weaker signal intensities (Fig. 6). CHIRPSv2 data adequately described precipitation regimes during the examination period (1981-2018) and for the majority of stations when compared with the ground precipitation data.

For the three-grid monthly series, the box plots (Fig. 7a and b) indicate RMSE values ranging from 52 to 223 mm and bias values between 141 and 168 mm. Figure 8a shows the dispersion of the KGE values between global products and observations, which increases from 0.30 (MSWEP and ERA5) to 0.46 (CHIRPSv2). Figure 8a demonstrates that all of the Pearson coefficients are positive, with median values of 0.41 (MSWEP), 0.42 (ERA5), and 0.58 (CHIRPSv2).

Figure 8c shows median values for β of 0.91 (MSWEP), 1.03 (ERA5), and 0.84 (CHIRPSv2). ERA5 overestimates precipitation, whereas MSWEP and CHIRPSv2 underestimate it. The median γ values are 0.85 (MSWEP), 0.89 (ERA5), and 0.80 (CHIRPSv2), and the interquartile range amplitudes in Fig. 8d show that a significant portion of the data underestimates the variability of precipitation observed on the ground. The spatial distribution of the mean annual precipitation in Haiti over the period 1980-2021 is shown in Fig. 9.

Preprint not peer reviewed

This preprint research paper has not been peer reviewed. Electronic copy available at: https://ssrn.com/abstract=5243924

These results show asymmetrical distributions for the four derived indices; however, the spatial characteristics of EOF1, high r coefficient values, and smaller dispersion of β and γ values suggest better performance for CHIRPSv2. These findings support the retention of this global dataset for the duration of this study.

3.2 Precipitation Regimes

3.2.1 Clustering analysis: Identification of Precipitation Regimes (PR)

PCA was followed by HAC, which used CHIRPSv2 monthly totals converted into the Standard Precipitation Index to divide Haiti geographically into four distinct zones (Fig. 10). PCA preserved the first 19 axes, which accounted for 95% of the initial inertia. The ideal dendrogram was obtained at c = 4. The monthly totals were then organized by region using the K-MED approach. The silhouette index showed an optimal number of clusters of seven, as evidenced by the change in the slope of the curve depicting the evolution of the average score of the silhouette index as a function of the number of clusters k, with k = 7 yielding an average score of 0.4 (Fig. 11).

Figures 12 and 13 illustrate the spatial distribution of the monthly isohyets for the obtained paragons, as well as the annual distribution of the months constituting these seven clusters. These two figures, combined with the statistical parameters in Table 3, allow the classification of these clusters into three precipitation regime (PR) groups.

Clusters 3, 1, and 5 formed a group of rainy regimes (RR). These were designated RR1, RR2, and RR3, with spatial monthly averages of 91.5, 140.8, and 220 mm, respectively. These three regimes accounted for 57.1% (273 of 480 months) of the monthly totals, with RRs of 18.5%, 26.7%, and 11.9%, respectively. RR2 and RR3 were characterized by monthly isohyets exceeding 120 mm, which covered most of the country. Temporally, the monthly distributions were as follows: April to November for RR1, March to December for RR2, and May to October for RR3 (Fig. 13). The maximum occurrences found in May and September-October suggested that RR2 and RR3 coincided with the two major rainy periods, the ERS and LRS. For RR1, the highest occurrences appear in April and July. The coefficient of variation was approximately 30% (Table 3). The minimum, maximum, and quartile values of the totals suggested more stable and predictable PRs for RR1 and RR2. For RR3, the amplitude between the minimum and maximum monthly totals and a significant standard deviation, indicate a more unpredictable and potentially intense regime.

Preprint not peer reviewed

This preprint research paper has not been peer reviewed. Electronic copy available at: https://ssrn.com/abstract=5243924

The Dry Regimes (DR) group, which included Clusters 4, 2, and 6, accounted for 37.6% of the global dataset (180 of 480 months). They are classified as DR1, DR2, and DR3 from the driest to the wettest. These account for 17.1%, 7.1%, and 13.4% of all monthly totals. The monthly spatial averages were 31, 44.2, and 54.8 mm. They occur less frequently and are two to seven times less rainy than the RRs. The spatial distribution of DR totals is marked by low precipitation throughout the country but is generally higher in northern Haiti, particularly in DR3. They were preferentially observed from November of year n to April of year n+1, corresponding to the WDS (Fig. 13). The highest incidences were recorded in January for DR1, March for DR2, and December for DR3. High coefficients of variation (> 50%) confirmed that the variability increased as the monthly totals decreased.

The seventh cluster, named the Intermediate Regime (IR), accounted for only 5.4% of the total dataset (26 of 480 months) and had a spatial average of 71.1 mm. This regime corresponds to moderate to low precipitation on the peninsula and significantly higher precipitation in the center of the country. The coefficient of variation (39.2%) was comparable to that of RRs. The IR occurred more frequently in June and July.

3.2.2 Seasonal and Interannual Variability

The monthly distribution of the seven identified regimes over 40 years enabled the evaluation of potential sequences related to seasonal and interannual variations (Fig. 14). The sequences were ranked in ascending order from the driest years (< 976 mm) to the wettest (> 1442 mm). The categorical classification clearly distinguished between the WDS (light red to yellow), ERS/LRS (blue to dark blue), and MSD (orange) seasons. These regimes illustrate the various stages of the annual precipitation cycles in Haiti.

Dry years include 1989, 2013, 2014, 2015, and 2019. These findings are consistent with previously reported drought periods in the region, including 1985-1993 and 2013-2015 (Herrera and Ault 2017; Hernández-Ayala and Heslar 2019). In April-May and October-November, DR- and RR1-type PRs prevail, whereas in June, the transitional regime (IR) predominates. High monthly totals for the RR3 type are rare. These temporal sequences result in fairly dry ERS.

The wet year sequences (1993, 2005, 2007, 2010, and 2017) are distinguished by numerous occurrences of RR-type regimes that embed themselves in the WDS beginning in March and ending with a predominance of RR2 in April. The presence of

Preprint not peer reviewed

This preprint research paper has not been peer reviewed. Electronic copy available at: https://ssrn.com/abstract=5243924

RR3 during this period causes wet ERS and LRS. Martinez et al. (2019) also found wet LRS in the same years.

The probability of transitioning from one regime to another was calculated to assess the dynamic behavior of the historical data system. Table 4 lists these values.

1. The probability of staying in the initial state was higher for DR1 (0.49) and RR2 (0.40). Except for DR2, which has the lowest score (0.12), the probabilities range from 0.2 to 0.25.
2. Intra-regime transitions between DR-type regimes (from DR3 to DR1, 0.47) and RR-type regimes (from RR3 to RR2, 0.41) were both possible and frequent.
3. Transitions between regimes were generally less frequent. The highest probabilities were observed when transitioning from DR2 to RR1 (0.44) or RR2 (0.32). The IR regime preferentially evolved towards rainy regimes such as RR1 (0.39).
4. No transitions from the dry regime (DR) to IR or RR3 were observed. The same applies to the transition from the rainy regime (RR) to DR2.

3.3 Teleconnections

The chi-square test (Table 5) revealed a statistically significant relationship between the PR and ENSO phases (Niña, neutral, and Niño). The p-value was < 0.001. Some PRs occur more or less frequently depending on the phase. The standardized residuals indicate discrepancies in the contingency table. During La Niña, the frequencies of IR (-2.17) and RR1 (-2.87) decrease. In neutral conditions, DR1 (-2.8) and DR3 (-2.41) decrease, while RR1 (2.71) increases. During El Niño, the frequency of IR (2.16) and RR3 (-2.14) decrease. The dependence of the PR on the NAO was not significant. **3.4 Monthly Anomalies and Composites**

The fields of geopotential anomalies at 925 hPa, SST, TP, and the wind-total precipitation composites were plotted using the ERA-5 reanalysis for each type of regime (Figs. 15, 16, and 17). The climatological period 1981–2020 served as the reference period, and the selected spatial domains ranged from 100° W to 50° W and 5° N to 30° N.

Four large-scale spatial anomaly configurations of the 925 hPa geopotential were associated with the PR (Fig. 15). These zones were spatially defined and featured

Preprint not peer reviewed

This preprint research paper has not been peer reviewed. Electronic copy available at: https://ssrn.com/abstract=5243924

opposite signs. The pairs with comparable but opposite anomalies are DR2-RR2, DR3-RR1, and DR1-RR3. The predominant zonal anomaly spanned the majority of the investigated domains, from the Eastern Pacific Ocean to the North Atlantic, passing through the southern Gulf of Mexico. The IR differs in that it exhibits a positive and strong geopotential anomaly in the northeastern Atlantic.

The TP anomalies associated with the PR had predominantly positive and negative configurations for the RR and DR types, respectively (Fig. 16). Positive anomalies in the RR were concentrated in the center around the Antilles and southern South America, with the exception of RR1, which displayed negative anomalies from southern Haiti to the CLLJ region (Fig. 16, left). Negative anomalies dominate the DR and increase towards the equator (Fig. 16, right). DR3, the wettest dry regime, has modest anomalies near the climatological mean of the TP, including a small positive anomaly in the CLLJ region. In the IR, the spatial model shows a dipole with a zonal band of negative anomalies from the North Atlantic that spans the Greater Antilles and curves toward Colombia and Venezuela.

The mean wind patterns at 925 hPa show a divergent easterly flow over the Caribbean Sea, which divides into two branches near Central America. In dry regimes, the upper branch flows southeast but weakens over the Gulf of Mexico before turning northward and westward in the upper layers. The lower branch moves northeast and intensifies as it enters the eastern Pacific Ocean. During this time, the CLLJ activity was high, and the ITCZ was located south of 10° N, which increased the upwelling of cooler waters and resulted in negative SST anomalies along the Venezuelan coast, particularly for DR1 and DR3. In RR-type regimes, trade winds are east-southeast oriented, with less severe Caribbean divergence and a weaker lower branch. A weak divergence-convergence dipole was found in the Pacific Ocean as the ITCZ shifted northward. The mean wind field in the IR regime was similar to that in the rainy regimes.

Warm and cold anomalies in SST developed from the three maritime basins, the Caribbean Sea, North Atlantic, and Eastern Pacific, depending on the type of regime (Fig. 17). The anomaly was completely positive for the rainy RR type. It becomes negative in dry conditions in the northern part of the domain for the dry DR type.

Preprint not peer reviewed

This preprint research paper has not been peer reviewed. Electronic copy available at: https://ssrn.com/abstract=5243924

4. Discussion

The flexible framework described in this study enables the estimation of precipitation regimes for the island territory of Haiti from 1981 to 2020 using a new classification method based on the spatial distributions of monthly totals from the global CHIRPSv2 dataset (5 km resolution). Monthly precipitation totals were divided into seven clusters known as regimes, which included dry, wet, and intermediate types. Moron et al. (2015) found just four clusters in Haiti. This difference can be explained by the use of the k-means classification, which, because it is based only on the L2 distance, can group monthly totals with extremely diverse temporal and spatial precipitation trends (Biabiany et al., 2022). Furthermore, other factors, such as orography and/or the existence of a typically opposing signal between weather stations in the northwest of the Caribbean and other stations in the region, complicate the analysis of rainfall variability in the area (Giannini et al., 2001; Chen and Taylor, 2002; Herrera and Ault, 2017).

The limits in performance, quality, and representativeness of the data.

The high variance values for the EOFs (Fig. 5) suggest that the ground stations and CHIRPSv2 grid cells share a common interannual signal, which may be reasonably estimated using the spatiotemporal distributions of the CHIRPSv2 dataset. Using D_{KL} instead of the L2 distance resulted in a better grouping of precipitation distributions in this region. D_{KL} is associated with dual-affine connections derived from distribution mixes using addition and/or exponential combinations (Amari and Nagaoka, 2000). These methods have proven useful and effective in distinguishing the distribution of a conjugated variable (precipitation) caused by various parameters that can be added and/or multiplied by complex interactions among the atmosphere, ocean, and orography. However, the choice of using D_{KL} instead of L2 distance for grouping precipitation distributions, while beneficial, may also introduce complexities that could affect the interpretation of results. The reliance on specific statistical methods may limit the generalizability of the findings to other contexts or regions.

The monthly CHIRPSv2 data adequately reflect the oscillatory variability of 0.5 years and 1 year. However, the data from the ground stations showed a slightly higher and

Preprint not peer reviewed

This preprint research paper has not been peer reviewed. Electronic copy available at: https://ssrn.com/abstract=5243924

more consistent energy behavior than the CHIRPSv2 data. In terms of interannual variability, the monthly precipitation results were well represented, with only minor discrepancies amongst the stations studied. This discrepancy suggests that while CHIRPSv2 is useful, it may not always align perfectly with ground observations, potentially leading to underestimations or misrepresentations of precipitation patterns.

This spatial heterogeneity in Haiti results in distinct oscillatory patterns depending on the region (South, West, and North). The station-based study revealed that the dominant 1-year energy band at Cap Haitien (northern region) weakened significantly from 1981 to 1997 in CHIRPSv2 data, but not in ground station data. In contrast, for the Port-au-Prince (western region) and Cayes (southern region) ground stations, the robust 1-year power spectrum in the CHIRPSv2 data dominated the long-term variability, with high and continuous energy throughout the investigated period. For long-term interannual variability (3-7 years), the CHIRPSv2 data recreated a variability pattern with lower oscillatory representation quality. The three ground stations experienced a 30–60-month oscillation, comparable to large-scale atmospheric-oceanic phenomena such as the Southern Oscillation of the Niño-ENSO. The wavelet power spectra of the CHIRPSv2 data showed weak energies.

The KGE and triplet (r, β, γ) orders of magnitude indicate a good fit between CHIRPSv2 and rain gauge data for both periods investigated. The calculated values are comparable with those found in studies by Cantella et al. (2020) and Bathélémy et al. (2022) for the Caribbean, as well as Sun et al. (2017) in their analysis of global products for South America. Meanwhile, as suggested by Du et al. (2023), we believe that in the absence of ground stations, CHIRPS can be used to calculate hydrometeorological variables specific to this geographical area under different climatic conditions. These findings are a good test of the quality and representativeness of the CHIRPSv2 dataset for Haiti, demonstrating that CHIRPSv2 is an accurate estimator of precipitation trends. The global results are consistent with the climatology of the country. The intra-annual variability (0.5 y) confirms the influence of high-pressure centers and the ITCZ on Haiti's climatology. From 1981 to 2018, two maximum rainfall peaks (bimodality) were detected in May and September-October (rainy season), as well as two minimum rainfall troughs in January and July (dry season).

Changes in annual PR sequences from 1981 to 2020

Preprint not peer reviewed

This preprint research paper has not been peer reviewed. Electronic copy available at: https://ssrn.com/abstract=5243924

The various monthly and annual totals illustrate that the CHIRPSv2 dataset includes ENSO and NAO phase signatures. Similar results have been reported from South America (López-Bermeo et al., 2022; Du et al., 2023). Our findings demonstrated that these phases never resulted in exactly the same transitions and thus the same meteorological and climatic effects in Haiti. The transitions and changes in this dataset can be interpreted as the repetition of precipitation regimes since 1981, with persistence and/or shifts to other types explaining the annual or even multiannual effects on totals. The dry season, or its transition to the interseason, is represented by DR1 to DR3 transitions from 1991 to 2000, whereas DR1 remains in DR1 from 2001 to 2020. The dry season has little intra-annual variability compared to the rainy season.

The effects of anomaly fields and composites in Haiti

Composites combining precipitation (large-scale and convective) and wind fields reinforce and provide physical meaning to the classification results. To qualify the identified regimes, they were correlated with additional climatic parameters over an expanded spatial domain. Overall, the anomaly fields and composites generated by the seven regime groups accurately characterized the large-scale spatial variability. The presence of positive geopotential anomalies at 925 hPa in the DR weakened the climatological southeast winds and strengthened the CLLJ. As a result, cold air from North America is blocked as it moves towards the eastern Caribbean. The climatological divergence between Nicaragua and Costa Rica, particularly its strong southern branch, has resulted in dry regimes, including ERS that are dry (Jury et al., 2007; Allen and Mapes, 2017; Herrera and Ault, 2017; Martinez et al., 2021). Negative anomalies, which are typical of RR regimes, coincided with the strengthening of climatological southeast winds in the Caribbean Sea (RR2 and RR3). The divergence in the east–southeast flow occurred primarily southwest of Haiti. CLLJ activity promotes the upward movement of cooler water towards Haiti, lowering SSTs and causing negative precipitation anomalies south of the island. This was primarily owing to an increase in the westward expansion of the subtropical anticyclone in July and August, resulting in the MSD being the second lowest during the rainy season in this region.

Preprint not peer reviewed

This preprint research paper has not been peer reviewed. Electronic copy available at: https://ssrn.com/abstract=5243924

When focusing on Haiti (Fig. 18), using the 925 hPa isobar as an indicator of the eastward flow altitude allowed us to reduce the numerous orographic effects caused by Haiti's unique shape without eliminating some local effects (Daly et al., 2003). Wind vectors represent low-altitude convergence (associated with ascent and precipitation) or divergence (associated with subsidence and dry conditions), which affects precipitation.

Figure 18 shows a common wind circulation pattern for the seven regimes, with the easterly flow splitting around Hispaniola and weakening in central and northwest Haiti at 925 hPa. The flow was significantly reduced in the center and northwest tips of Haiti. To the south, on the Caribbean coast, the flow direction remained from east to southeast for all regimes. Except for RR1, all rainfall regimes have TP anomaly halos that intensify from sea to land due to convection, convergence, and/or the upward motion of humid maritime air, as well as local orographic effects.

The RR2-3 and DR2-3 regimes share several TP anomaly zones downwind of the E-NE trade winds, particularly in the northern peninsula, Artibonite Valley, central Haiti, and Cul-de-Sac Plain. For RR2 and RR3, the dominant positive anomalies in the southern peninsula are caused by a combination of depression systems passing through this area and the orographic effects of the Hotte Mountain slopes, which facilitate significant rainfall accumulation. The shorter northern peninsula and lower mountain ranges in the north have resulted in less intense mechanisms, causing a significant precipitation asymmetry between the two locations. Precipitation occurs mainly over the sea and is more widespread but less intense.

DR3 was unique among dry regimes, with a dipole (-/+) on the northern coast and positive anomalies covering a large maritime area due to the prevalence of large-scale precipitation (cold fronts). In wet regimes, a zone of dry (wet) anomalies develops in the Central Plateau region, upwind from the Central Cordillera. Heat and humidity from the lower atmosphere of the Gulf of Gonâve, along with easterly circulations, are likely to generate severe convection even without large-scale precipitation systems.

In Haiti, the transition from a dry to a wet SST configuration occurs gradually, with meridional gradients that generally reverse depending on the regime. Colder-than-average SSTs in the southern Caribbean Sea were associated with increased easterly winds and lower monthly totals in Haiti (DR1 and DR2). Local ocean-atmosphere couplings between CLLJ speeds and warmer Caribbean waters moving northward into

Preprint not peer reviewed

This preprint research paper has not been peer reviewed. Electronic copy available at: https://ssrn.com/abstract=5243924

the Greater Antilles can produce DR3-like conditions, resulting in slightly wetter dry seasons.

Seasonal transitions and regional differences in rainfall.

The examination of the geographic distribution of rainfall, precipitation variation with latitude, and the regularity of short- and long-term oscillatory patterns at several geographical points enabled Haiti to be divided into four rainfall regions. The CHIRPSv2 time series prompted us to suggest and characterize small-scale precipitation regimes in this region. Our analysis reveals that a calendar year can be divided into four (rainy years) or six (dry years) regimes. These findings did not contradict the bimodal seasonal cycles described in previous studies. Using finer spatial resolutions (0.05° x 0.05°) and identifying these regimes, we were able to highlight seasonal transitions and explain potential regional differences in the Caribbean. In the absence of ground stations, it is hypothesised that CHIRPS can be used to calculate hydrometeorological variables specific to this territory. These calculations should be made in conjunction with hydrological models for hydrological research, and under different climatic conditions.

5. Conclusion

Haiti faces challenges in managing water resources and predicting floods and droughts, owing to a lack of high-resolution rainfall data. Freely accessible gridded precipitation products have the potential to fill these gaps while also providing the advantages of wide spatial coverage and temporal continuity. This study used CHIRPSv2 data (5 km resolution) to investigate precipitation variability from 1981 to 2020. Classification methods identified four spatially coherent rainfall zones and seven spatiotemporal distributions that distinguished the basic building blocks of dry (DR1, DR2, and DR3) and wet (RR1, RR2, and RR3) periods as well as MSD-induced rainfall regression (IR). The RR-type regimes showed a monthly distribution that included both wet seasons (ERS and LRS).

The estimated transition probabilities indicate significant variability in annual sequences, revealing the lack of a unique annual model linked with a specific set of regimes in Haiti. This result suggests that abnormally dry or wet years cannot be systematically linked to specific intra-annual scenarios.

Preprint not peer reviewed

This preprint research paper has not been peer reviewed. Electronic copy available at: https://ssrn.com/abstract=5243924

Examining the anomalies and large-scale atmospheric and oceanic composite fields confirmed that these regimes correspond to short-period atmospheric physical states. NASH, CLLJ, and the meridional SST gradient in the Caribbean Basin all had a substantial influence on the observed variability in the identified groupings.

There was no consistent annual pattern linking precipitation variability to large-scale climate factors such as ENSO and NAO. The CHIRPSv2 proved to be a dependable tool for monitoring rainfall changes and assisting with water resource management, agriculture, and climate adaptation in Haiti. This study's findings have implications for forecasting the variability in the two rainy seasons in Haiti. Furthermore, insights gained from Haiti provide a local perspective on broader seasonal and interannual rainfall variability patterns in the Greater Antilles.

Preprint not peer reviewed

This preprint research paper has not been peer reviewed. Electronic copy available at: https://ssrn.com/abstract=5243924

Acknowledgements:

The authors would like to acknowlege Marcelin Esterlin, Director of the Hydrometeorological Unit of Haiti and Permanent Representative of Haiti to the World Meteorological Organisation, for his strategic guidance and expert input, Jean-Noël Degrace, international expert in hydro-meteorological and climate risk management and early warning systems, for his thoughtful analysis, expert advice and constant encouragement based on his extensive experience with the World Meteorological Organization and the World Bank in the Caribbean and especially in Haiti, and Fabrice Sextus, instrumentation technician, for his availability. The authors have declared no competing interests.

Author contributions:

Didier Bernard: Conceptualization, Methodology, Software, Investigation, Formal analysis, Writing - original draft- review & editing, Project administration. **Romual Chery**: Investigation, Formal analysis, Data curation, Methodology, Software, Writing -review & editing. **Emmanuel Biabiany**: Software, Methodology, Data curation, Writing - review & editing. **Raphaël Cécé**: Methodology, Visualization, Writing - review & editing,

Funding sources:

Not applicable

Preprint not peer reviewed

This preprint research paper has not been peer reviewed. Electronic copy available at: https://ssrn.com/abstract=5243924

References

Alpert, L., 1942. Rainfall maps of Hispaniola. Bulletin of the American Meteorological Society, 423-431.

Amari, S., Nagaoka, H., 2000. Methods of information geometry, vol. 191, American Mathematical Society. https://doi.org/10.1090/mmono/191.

Angeles, M.E., González, J.E., Ramírez-Beltrán, N.D., Tepley, C.A., Comarazamy, D.E., 2010. Origins of the Caribbean rainfall bimodal behavior. J. Geophys. Res. Atmospheres 115. https://doi.org/10.1029/2009JD012990.

Allen, T.L., Mapes, B.E., 2017. The late spring Caribbean rain-belt: climatology and dynamics. Int. J. Climatol., 37(15), 4981-4993. https://doi.org/10.1002/joc.5136

Bathelemy, R., Brigode, P., Boisson, D. & Tric, E., 2022. Rainfall in the Greater and Lesser Antilles: Performance of five gridded datasets on a daily timescale. J. Hydrol. Reg. Stud., 43, 101203. https://doi.org/10.101DR3/j.ejrh.2022.101203.

Bathelemy, R., Brigode, P., Andréassian, V., Perrin, C., Moron, V., Gaucherel, C., Tric, E., and Boisson, D., 2024. Simbi: historical hydro-meteorological time series and signatures for 24 catchments in Haiti, Earth Syst. Sci. Data, 16, 2073–2098, https://doi.org/10.5194/essd-16-2073-2024.

Beck, H.E., Dijk, A.I.J.M., van, Levizzani, V., Schellekens, J., Miralles, D.G., Martens, B., de Roo, A., 2017. MSWEP: 3-hourly 0.25◦ global gridded precipitation (1979-2015) by merging gauge, satellite, and reanalysis data. Hydrol. Earth Syst. Sci., 21, 589–615. https://doi.org/10.5194/hess-21-589-2017.

Bernard, D., Biabiany, E., Cécé, R., Chery, R., Sekkat, N., 2022. Clustering analysis of the Sargassum transport process: application to beaching prediction in the Lesser Antilles. Ocean Sci. 18:915–935. https://doi.org/10.5194/os-18-915-2022.

Biabiany, E., Bernard, D., Pagé, V., Paugam-Moisy, H., 2020. Design of an expert distance metric for climate clustering: The case of rainfall in the Lesser Antilles. Comput. Geosci. 145, 104612, https://doi.org/10.1016/j.cageo.2020.104612.

Centella-Artola, A., Bezanilla-Morlot, A., Taylor, M.A., Herrera, D.A., Martinez-Castro, D., Gouirand, I., Sierra-Lorenzo, M., Vichot-Llano, A., Stephenson, T., Fonseca, C., Campbell, J., Alpizar, M., 2020. Evaluation of Sixteen Gridded Precipitation Datasets over the Caribbean Region Using Gauge Observations. Atmosphere, 11(12), 1334. https://doi.org/10.3390/atmos11121334.

Chen, A.A., Taylor, M.A., 2002. Investigating the link between early season caribbean rainfall and EL Nino+1 year. Int. J. Climatol. 22, 87-106. https://doi.org/10.1002/joc.711.

Copernicus Climate Change Service (C3S) Climate Data Store (CDS), DOI: 10.24381/cds.adbb2d47 (Accessed on 04-Jul-2024)

Copernicus Climate Change Service (C3S) Climate Data Store (CDS), DOI: 10.24381/cds.6860a573 (Accessed on 04-Jul-2024)

Preprint not peer reviewed

This preprint research paper has not been peer reviewed. Electronic copy available at: https://ssrn.com/abstract=5243924

Curtis S., Gamble D., 2008. Regional variations of the Caribbean mid-summer drought. Theor. Appl. Climatol. 94, 25–34. https://doi.org/10.1007/s00704-007-0342-0.

Daly, C., Helmer, E.H. and Quiñones, M., 2003. Mapping the climate of Puerto Rico, Vieques and Culebra. Int. J. Climatol., 23, 1359-1381. https://doi.org/10.1002/joc.937.

Du, H., Tan, M.L., Zhang, F., Chun, K.P., Li, L., Kabir, M.H., 2024. Evaluating the effectiveness of CHIRPS data for hydroclimatic studies. Theor. Appl. Climatol 155, 1519–1539. https://doi.org/10.1007/s00704-023-04721-9

Elusma, M., Tung, C. P., Lee, C. C., 2022. Agricultural drought risk assessment in the Caribbean region: the case of Haiti. International Journal of Disaster Risk Reduction, 83, 103414. https://doi.org/10.1016/j.ijdrr.2022.103414.

Enfield D.B., Alfaro E.J., 1999. The Dependence of Caribbean Rainfall on the Interaction of the Tropical Atlantic and Pacific Oceans. J. Climate 12:2093–2103. https://doi.org/10.1175/1520-0442(1999)012<2093:TDOCRO>2.0.CO;2.

Eisenberg, M. C., Kujbida, G., Tuite, A. R., Fisman, D. N., & Tien, J. H., 2013. Examining rainfall and cholera dynamics in Haiti using statistical and dynamic modeling approaches. Epidemics, 5(4), 197-207. https://doi.org/10.1016/j.epidem.2013.09.004.

ECMWF Reanalysis v5 (ERA5), https://www.ecmwf.int/en/forecasts/dataset/ecmwf-reanalysis-v5

FAO. 2024. Haiti: Executive brief of the DIEM-Monitoring assessment,round 5 (January 2024). Livelihoods at risk due to the effects of El Niñocompounded by an upsurge in violence. Rome. https://doi.org/10.4060/cd0293en

Funk, C., Peterson, P., Landsfeld, M., Pedreros, D. Verdin, J., Shukla, S., Husak G., Rowland, J., Harrison, L., Hoell, A., Michaelsen, J., 2015. The climate hazards infrared precipitation with stations—a new environmental record for monitoring extremes. Sci Data, 2,150066. https://doi.org/10.1038/sdata.2015.66.

Gamble, D.W., Curtis S., 2008. Caribbean precipitation: review, model and prospect. Progress in Physical Geography: Earth and Environment 32, 265-276. https://doi.org/10.1177/0309133308096027.

Giannini, A., Kushnir, Y., Cane, M. 2000. Interannual Variability of Caribbean Rainfall, ENSO, and the Atlantic Ocean. J. Clim. 13, 297–311. https://doi.org/10.1175/1520/0442(2000)013<0297:IVOCRE>2.0.CO;2.

Giannini, A., Chiang. J.C.H., Cane, M.A., Kushnir, Y., Seager, R., 2001.The ENSO Teleconnection to the Tropical Atlantic Ocean: Contributions of the Remote and Local SSTs to Rainfall Variability in the Tropical Americas. J. Climate 14, 4530–4544. https://doi.org/10.1175/1520-0442(2001)014<4530:TETTTT>2.0.CO;2.

Gouirand, I., Jury, M.R., Sing, B., 2012. An Analysis of Low- and High-Frequency Summer Climate Variability around the Caribbean. Antilles. J. Climate, 25, 3942–3952. https://doi.org/10.1175/JCLI-D-11-00269.1.

Preprint not peer reviewed

This preprint research paper has not been peer reviewed. Electronic copy available at: https://ssrn.com/abstract=5243924

Gouirand, I., Moron, V., Hu, Z.Z., Jha, B., 2014. Influence of the warm pool and cold tongue El Niños on the following Caribbean rainy season rainfall. Clim. Dyn., 42, 919–929. https://doi.org/10.1007/s00382-013-1753-5.

Gouirand, I., Moron, V, Sing B., 2020. Seasonal atmospheric transitions in the Caribbean basin and Central America. Clim Dyn. 55, 1809–1828. https://doi.org/10.1007/s00382-020-05356-6.

Gouirand, I., Moron, V., Sing, B., 2024. Defining a Caribbean regional-scale mid-summer drought based on weather types from 1950 to 2021. Clim. Dyn. 62, 3977–4000. https://doi.org/10.1007/s00382-024-07111-7.

Gu, G., Adler, R.F., 2006. Interannual rainfall variability in the tropical Atlantic region. J. Geophys. Res. 111, D02106. https://doi.org/10.1029/2005JD005944.

Gupta H.V., Kling H., Yilmaz K.K., Martinez G.F., 2009. Decomposition of the mean squared error and NSE performance criteria: Implications for improving hydrological modelling. Journal of hydrology. 377, 80-91. https://doi.org/10.1016/j.jhydrol.2009.08.003.

Hernández Ayala JJ, Heslar M, 2019. Examining the spatiotemporal characteristics of droughts in the Caribbean using the standardized precipitation index (SPI). Clim Res 78,103-116. https://doi.org/10.3354/cr01562.

Herrera, D., and Ault, T., 2017. Insights from a new high-resolution drought atlas for the Caribbean spanning 1950 to 2016. Journal of Climate, 30, 7801–7825. https://doi.org/10.1175/JCLI-D-16-0838.1.

Herrera, D., Ault, T.R;, Fasullo, J.T., Coats, S.J., Carrillo, C.M., Cook, B.I., Williams, A.P., 2018. Exacerbation of the 2013–2016 Pan-Caribbean drought by anthropogenic warming. Geophysical Research Letters. 45,10,619–10,626. https://doi.org/10.1029/2018GL079408 .

Hersbach, H., Bell, B., Berrisford, P., Hirahara, S., Horány,i A., Muñoz-Sabater, J., Nicolas, J., Peubey, C., Radu, R., Schepers, D., Simmons, A., Soci, C., Abdalla, S., Abellan, X., Balsamo, G., Bechtold, P., Biavati, G., Bidlot, J., Bonavita, M., De Chiara, G., Dahlgren, P., Dee, D., Diamantakis, M., Dragani, R., Flemming, J., Forbes, R., Fuentes, M., Geer, A., Haimberger, L., Healy, S., Hogan, R.J., Hólm, E., Janisková, M., Keeley, S., Laloyaux, P., Lopez, P., Lupu, C., Radnoti, G., de Rosnay, P., Rozum, I., Vamborg, F., Villaume, S., Thépaut, J.-N., 2020. The ERA5 global reanalysis. Q. J. R. Meteorol. Soc. 146, 1999–2049. https://doi.org/10.1002/qj.3803

Jones, P.D., Harpham, C., Harris, I., Goodess, C.M., Burton, A., Centella-Artola, A., Taylor, M.A., Bezanilla-Morlot, A., Campbell, J.D., Stephenson, T.S., Joslyn, O., Nicholls, K., Baur, T., 2016. Long-term trends in precipitation and temperature across the Caribbean. Int. J. Climatol. 36, 3314-3333. https://doi.org/10.1002/joc.4557

Jury, M.R., Malmgren, B.A., Winter, A., 2007. Sub-regional precipitation climate of the Caribbean and relationships with ENSO and NAO. J. Geophys. Res. 112, D16107. https://doi.org/ 10.1029/2006JD007541.

Preprint not peer reviewed

This preprint research paper has not been peer reviewed. Electronic copy available at: https://ssrn.com/abstract=5243924

Jury, M.R., 2009. An intercomparison of observational, reanalysis, satellite, and coupled model data on mean rainfall in the Caribbean. J. Hydrometeorol. 10, 413–430. https://doi.org/10.1175/2008JHM1054.1.

Jury, M.R., Gouirand, I., 2011. Decadal climate variability in the eastern Caribbean. J. Geophys. Res. 116, D00Q03. https://doi.org/10.1029/2010JD015107.

Jury, M.R., 2019. The pattern of climate change around the Windward Passage. Theor. Appl. Climatol. 137, 1149–1157. https://doi.org/10.1007/s00704-018-2658-3.

Jury, M.R., Bernard, D., 2020. Climate trends in the East Antilles Islands. Int. J. Climatol. 40, 36–51. https://doi.org/10.1002/joc.6191 .

Jury, M.R., 2023. Springtime Southwest Cloud Bands in the Central Caribbean. J. Appl. Meteor. Climatol., 62, 251–262. https://doi.org/10.1175/JAMC-D-22-0126.1.

Gupta, H.V., Kling, H., Yilmaz, K.K., and Martinez, G.F., 2009. Decomposition of the mean squared error and NSE performance criteria: Implications for improving hydrological modelling, J. Hydrol., 377, 80–91, https://doi.org/10.1016/j.jhydrol.2009.08.003,

Kaufman, L., & Rousseeuw, P. J., 2009. Finding groups in data: an introduction to cluster analysis. John Wiley & Sons.

Kullback S., Leibler R.A., 1951. On information and sufficiency. The annals of mathematical statistics. 22(1), 79-86.

Laing, A.G., 2004. Cases of Heavy Precipitation and Flash Floods in the Caribbean during El Niño Winters. J. Hydrometeor. 5, 577–594, https://doi.org/10.1175/1525-7541(2004)005<0577:COHPAF>2.0.CO;2.

López-Bermeo, C., Montoya, R.D., Caro-Lopera, F.J., Díaz-García J.A., 2022. Validation of the accuracy of the CHIRPS precipitation dataset at representing climate variability in a tropical mountainous region of South America. Physics and Chemistry of the Earth. 127, 1474-7065. https://doi.org/10.1016/j.pce.2022.103184.

Magaña, V., Amador, J.A., Medina, S., 1999. The midsummer drought over Mexico and Central America. J. Climate, 12, 1577–1588. https://doi.org/10.1175/1520 0442(1999)012<1577:TMDOMA>2.0.CO;2.

McKee T.B., 1995. Drought monitoring with multiple timescales. 9th Conference on Applied Climatology, American Meteorological Society Dallas, USA, 15-20 january 1995 ; 233–23DR3.

Martinez, C., Goddard, L., Kushnir, Y., Ting M., 2019. Seasonal climatology and dynamical mechanisms of rainfall in the Caribbean. Climate. Dyn. 53, 825–846, https://doi.org/10.1007/s00382-019-04616-4.

Martinez, C., Kushnir, Y., Goddard .L, Ting, M., 2020. Interannual variability of the early and late/rainy seasons in the Caribbean. Clim. Dyn. 55, 15DR33–1583. https://doi.org/10.1007/s00382-020-05341-z.

Preprint not peer reviewed

This preprint research paper has not been peer reviewed. Electronic copy available at: https://ssrn.com/abstract=5243924

Moron, V., Frelat, R., Jean-Jeune, P.K., Gaucherel, C., 2015. Interannual and intra-annual variability of rainfall in Haiti (1905–2005). Clim. Dyn. 45, 915–932. https://doi.org/10.1007/s00382-014-2326-y.

Moron, V., Gouirand, I., Taylor M., 2016. Weather types across the Caribbean basin and their relationship with rainfall and sea surface temperature. Clim. Dyn. 47, 601–621. https://doi.org/10.1007/s00382-015-2858-9.

NASA JPL. NASA Shuttle Radar Topography Mission Global 3 arc second sub-sampled. 2013, distributed by NASA EOSDIS Land Processes Distributed Active Archive Center, https://doi.org/10.5067/MEaSUREs/SRTM/SRTMGL3S.003. Accessed 2025-02-07.

Paca, V.H.d.M., Espinoza-Dávalos, G.E., Moreira, D.M., Comair, G., 2020. Variability of Trends in Precipitation across the Amazon River Basin Determined from the CHIRPS Precipitation Product and from Station Records. Water, 12, 1244. https://doi.org/10.3390/w12051244.

Pérez, C.R., Jury, M.R., 2013. Spatial and temporal analysis of climate change in Hispañola. Theor. Appl. Climatol. 113, 213–224. https://doi.org/10.1007/s00704-012-0781-0.

Rousseeuw, P.J., 1987. Silhouettes : A graphical aid to the interpretation and validation of cluster analysis. Journal of Computational and Applied Mathematic. 20,53-65. https://doi.org/10.1016/0377-0427(87)90125-7.

Roesch, A., Schmidbauer, H., 2018. WaveletComp: Computational Wavelet Analysis. R package version 1.1. https://CRAN.R-project.org/package=WaveletCom.

Singh, R. J., & Barton-Dock, M., 2015. Haiti: Toward a new narrative. Systematic country diagnostic. World Bank, Washington, DC (2015)

Sun, Q., Miao, C., Duan, Q, Ashouri, H., Sorooshian S., Hsu K., 2018. A Review of Global Precipitation Data Sets: Data Sources, Estimation, and Intercomparisons. Rev. Geophys. 56, 79–107. https://doi.org/10.1002/2017RG000574.

Taylor, M.A., Enfield D.B., Chen A.A., 2002. Influence of the tropical Atlantic versus the tropical Pacific on Caribbean rainfall. J. Geophys. Res. Oceans. 1107, 3127. https://doi.org/10.1029/2001JC001097.

Taylor, M.A., Stephenson T.S., Owino, A., Chen, A.A., Campbell, J.D., 2011. Tropical gradient influences on Caribbean rainfall. J. Geophys. Res. 116, D00Q08. https://doi.org/10.1029/2010JD015580.

Torrence, C., Compo G.P., 1998. A Practical Guide to Wavelet Analysis. Bull. Amer. Meteor. Soc., 79, 61–78, https://doi.org/10.1175/1520-0477(1998)079<0061:APGTWA>2.0.CO;2.

Zambrano-Bigiarini, M., Nauditt, A., Birkel, C., Verbist, K., & Ribbe, L., 2017. Temporal and spatial evaluation of satellite-based rainfall estimates across the complex topographical and climatic gradients of Chile. Earth Syst. Sci., 21, 1295–1320. https://doi.org/10.5194/hess-21-1295-2017.

Preprint not peer reviewed

This preprint research paper has not been peer reviewed. Electronic copy available at: https://ssrn.com/abstract=5243924

922 Wang, C. Variability of the Caribbean Low-Level Jet and its relations to climate . Clim
923 Dyn, 29, 411–422 . https://doi.org/10.1007/s00382-007-0243-z.
924

Preprint not peer reviewed

This preprint research paper has not been peer reviewed. Electronic copy available at: https://ssrn.com/abstract=5243924

List of tables

Table 1. Classes used to quantify monthly spatial distributions of precipitation from CHIRPSv2, during 1981 to 2020.

Min	Déciles (mm)									Max
	0,1	0,2	0,3	0,4	0,5	0,6	0,7	0,8	0,9	
1.3	19.17	31.76	46.50	62.40	79.6	99.4	122.9	154.2	205.9	1350.1

Table 2. Summary statistics of the annual precipitations (in *mm*) from the rain gauges: minimum (Min), first, second and third quartiles (q_1, q_2, q_3), 95th and 99th percentiles (q_{95}, q_{99}), standard deviation (σ), maximum (Max), interquartile range (q_3-q_1), coefficient of variation (CV) and data size (N).

1961-2018	Cap-Haitien	Ouanaminthe	Cayes	Jacmel	Ridorée	Port-au-Prince
Min	745.2	728.2	774.3	734.9	814.4	756.2
q_1	1127.4	1083	1362.7	1103.5	1154.2	1101.1
q_2	1402.1	1211.3	1641.6	1275.5	1398.3	1256.1
Mean	1410.3	1255.8	1690.6	1280.4	1418.1	1250.6
q_3	1621.2	1347.3	1947.4	1437.8	1559.2	1404.8
q_{95}	2063.7	1754.6	2654.8	1690.4	2049.4	1648.6
q_{99}	2300.4	2074.3	2759.7	2017.6	2395.4	1676.5
Max	2523.6	2116.5	2837.9	2127.5	2439	1687.6
q_3-q_1	493.8	264.25	584.75	334.3	405	303.76
σ	357.5	282.5	476.6	279.2	351.8	222.3
CV	0.25	0.22	0.28	0.21	0.24	0.18
N	673	689	689	693	671	690

Table 3. Summary statistics of the monthly precipitation regimes (in *mm*) identified in CHIRPSv2 data: minimum (Min), first, second and third quartile (q_1, q_2, q_3), mean, maximum (Max), standard deviation (σ), coefficient of variation (CV) and data size (N).

Regimes		Min	q_1	q_2	Mean	q_3	Max	σ	CV	N	%
C4	**DR1**	5.1	15.7	24.7	31.0	39.4	123.6	20.4	65.8	83	17.3
C2	**DR2**	6.8	25	41.4	44.2	62	111.7	22.6	51.1	33	6.9
C6	**DR3**	15.1	32	44.8	54.8	67.6	207.5	32.4	59.1	65	13.5
C7	**IR**	21.3	50.4	67.2	71.7	91.5	175.1	28.1	39.2	25	5.2
C3	**RR1**	29.3	69.7	92.7	91.5	110.7	202.9	29.7	32.4	89	18.5
C1	**RR2**	43.7	109	142.3	140.8	169.1	332.4	45.9	32.6	128	26.7
C5	**RR3**	84.4	169.1	219.4	220.1	257.6	569.7	70.7	32.1	57	11.9

Preprint not peer reviewed

This preprint research paper has not been peer reviewed. Electronic copy available at: https://ssrn.com/abstract=5243924

940 **Table 4.** Probability matrix of transition obtained for the precipitation regimes.

Regimes	DR1	DR2	DR3	IR	RR1	RR2	RR3
DR1	0.49	0.21	0.21	-	0.06	0.03	-
DR2	0.06	0.12	0.06	-	0.44	0.32	-
DR3	0.47	0.19	0.23	-	0.08	0.03	-
IR	0.04	-	0.04	0.19	0.39	0.19	0.15
RR1	0.05	-	0.09	0.11	0.22	0.38	0.15
RR2	0.03	-	0.14	0.04	0.17	0.40	0.22
RR3	-	-	0.05	0.12	0.21	0.41	0.21

941

942

943 **Table 5.** Distribution of different RPs across the three climatic conditions of ENSO: La
944 Niña, Neutral, and El Niño. The percentages indicate the proportion of each RP for each
945 of these conditions.

	ENSO phases				
	Nina	**Neutral**	**Nino**	**Total**	**p-value**[2]
Regimes					< 0.001
DR1	35%	34%	31%	83	
DR2	30%	55%	15%	33	
DR3	35%	34%	31%	65	
IR	8%	48%	44%	25	
RR1	14.6%	60.7%	24.7%	89	
RR2	28%	48%	24%	128	
RR3	26%	60%	14%	57	
Number of Phases	128	229	123	480	

[2]Pearson's Chi-Squared test

946

Preprint not peer reviewed

This preprint research paper has not been peer reviewed. Electronic copy available at: https://ssrn.com/abstract=5243924

Figure Captions:

Fig. 1. Topographic map of Haiti at 90 m scale (NASA JPL Shuttle Radar Topography Mission Global 3 arc second sub-sampled, last accessed: 7 February 2025) with rain gauge locations (red cross).

Fig. 2. Map of rain gauge locations (black cross) and grid points used in this study to validate CHIRPSv2 (red dots), MSWEP (cyan dots), and ERA5 (grey dots).

Fig. 3. Framework of the clustering analysis process. The black arrows denote the data stream, whereas the red arrows denote the process flow.

Fig. 4. Monthly averaged rainfall readings from the rain gauge network from 1981 to 2018, divided by region: north (Cap Haïtien and Ouanaminthe), west (Port-au-Prince), and south (Ridorée, Jacmel, and Les Cayes).

Fig. 5. Spatial diagrams of the first EOF mode for monthly rainfall time series for each database from 1981 to 1990 (62 grid points). The cumulative values collected at each grid point were normalized using the maximum value.

Fig. 6. Wavelet power spectrum — The white contour represents the 5% level of significance when compared to a white noise null. The black contour represents the 5% significance threshold estimated from Monte Carlo simulations using phase-randomized surrogate series. The cone of influence, which shows the region impacted by edge effects, is illustrated in transparency. The power color code ranges from blue (low) to red (high).

Fig. 7. Bias (left) and root mean square error (right) between CHIRPSv2, ERA5, and MSWEP data and nearest gauges from 1981 to 1990.

Fig. 8. Kling-Gupta efficiency (KGE), Pearson product-moment correlation (r), bias ratio of the modified Kling–Gupta efficiency (β), and variability (γ) of CHIRPSv2, ERA5, and MSWEP versus gauges at corresponding grid cells for two time series: 1981-1990.

Fig. 9. CHIRPSv2 yearly averaged rainfall (mm) from 1981 to 2020.

Fig. 10. Spatial distribution of the four clusters resulting from a hierarchical cluster analysis of SPI-12 (12-month accumulated precipitation index).

Fig. 11. Evolution of the SaMk silhouette index as a function of the number of clusters k: L2 method (black), ED method (red).

Fig. 12. Spatial distribution of the monthly cumulative rainfall (mm) for the seven regimes. The left-hand column shows the dry regimes (DR) and the intermediate regimes (IR), while the right-hand column shows the rainy regimes (RR).

Fig. 13. The annual distribution of monthly totals for the dry (DR), intermediate (IR), and rainy regimes (RR).

Preprint not peer reviewed

This preprint research paper has not been peer reviewed. Electronic copy available at: https://ssrn.com/abstract=5243924

Fig. 14. Inter-annual and intra-annual variability of the seven precipitation regimes, as well as the annual cumulative spatially averaged rainfall values. The table is sorted from top to bottom, with the driest years first and then the wettest years.

Fig. 15. Geopotential anomalies at 925 hPa for each of the seven recognized regimes. The anomaly is calculated using the mean geopotential height of monthly data (1981-2020) from the ERA5 reanalysis as a baseline. The rainy (RR) and intermediate regimes (IR) are on the left, the dry regimes (DR) are on the right, and the average SST is on the bottom right.

Fig. 16. Total precipitation anomalies (mm) with wind circulation at 925 hPa (vector m s^{-1}) for each identified regime. The rainy (RR) and intermediate regimes (IR) are on the left, the dry regimes (DR) are on the right, and the monthly average precipitation is on the bottom right.

Fig. 17. SST anomalies in Kelvin for the seven identified regimes. The anomaly is determined using the SST of all monthly data (1981-2020) from the ERA5 reanalysis as a baseline. The rainy (RR) and intermediate regimes (IR) are on the left, the dry regimes (DR) are on the right, and the average SST is on the bottom right.

Fig. 18. Composites of precipitation anomalies (mm) with wind circulation at 925 hPa (vector m s^{-1}) over Haiti for each regime. The rainy (RR) and intermediate regimes (IR) are on the left, whereas the dry regimes (DR) are on the right.

Preprint not peer reviewed

This preprint research paper has not been peer reviewed. Electronic copy available at: https://ssrn.com/abstract=5243924

Figure 1

Preprint not peer reviewed

This preprint research paper has not been peer reviewed. Electronic copy available at: https://ssrn.com/abstract=5243924

Figure 2

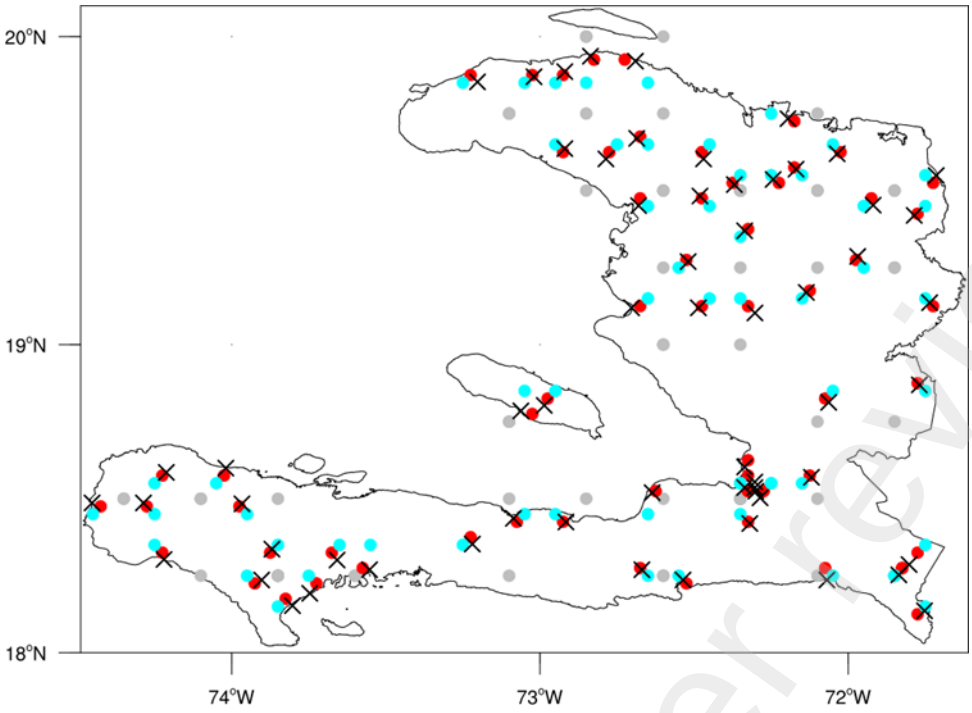

Preprint not peer reviewed

This preprint research paper has not been peer reviewed. Electronic copy available at: https://ssrn.com/abstract=5243924

Figure 3

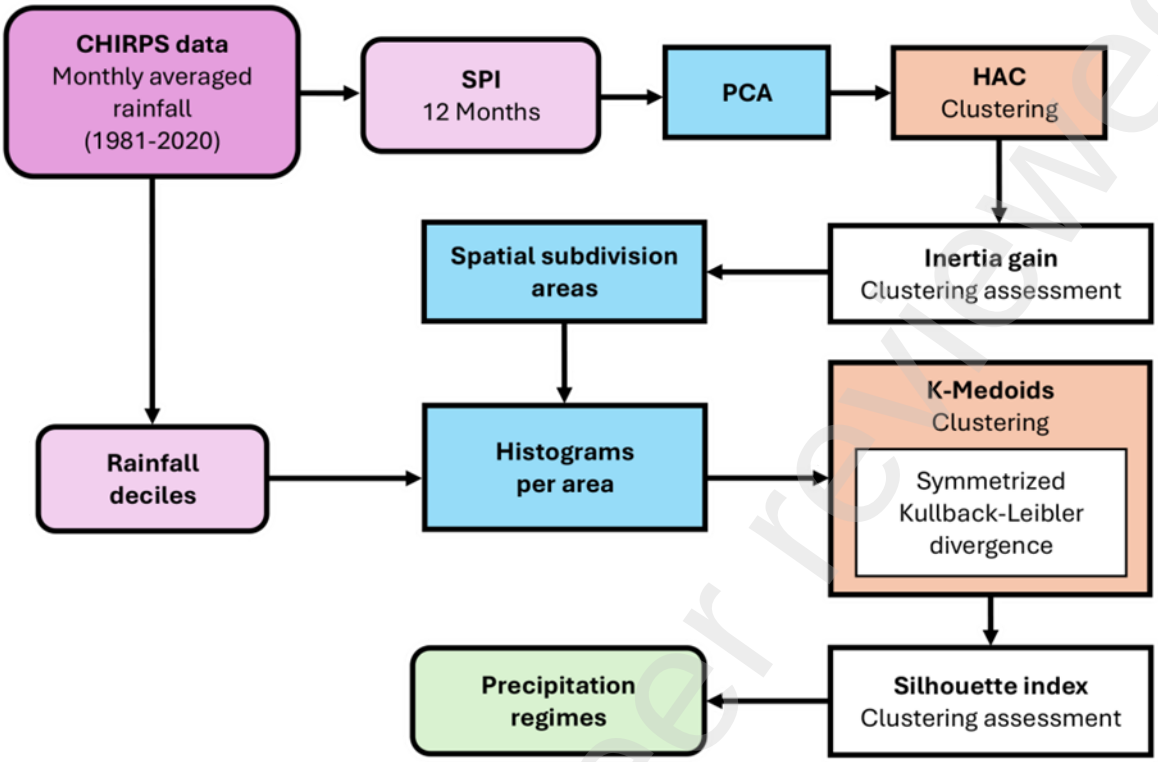

Preprint not peer reviewed

This preprint research paper has not been peer reviewed. Electronic copy available at: https://ssrn.com/abstract=5243924

Figure 4

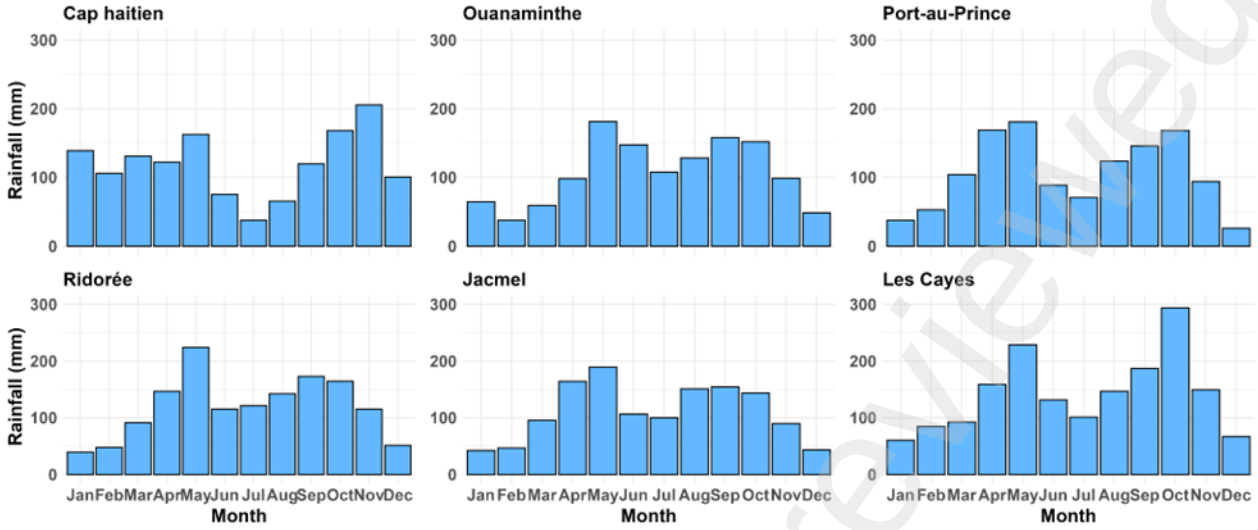

Preprint not peer reviewed

This preprint research paper has not been peer reviewed. Electronic copy available at: https://ssrn.com/abstract=5243924

Figure 5

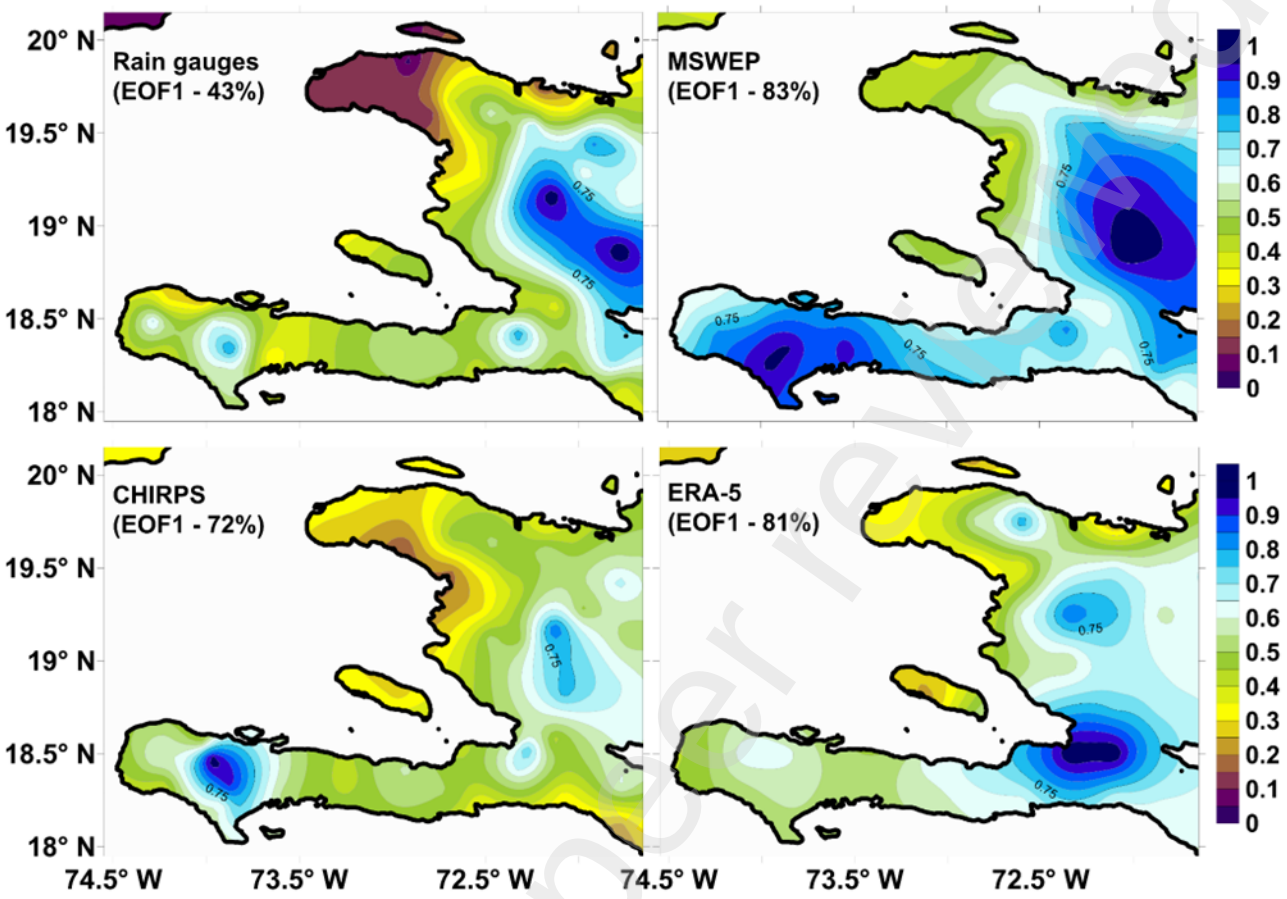

Preprint not peer reviewed

This preprint research paper has not been peer reviewed. Electronic copy available at: https://ssrn.com/abstract=5243924

Figure 6

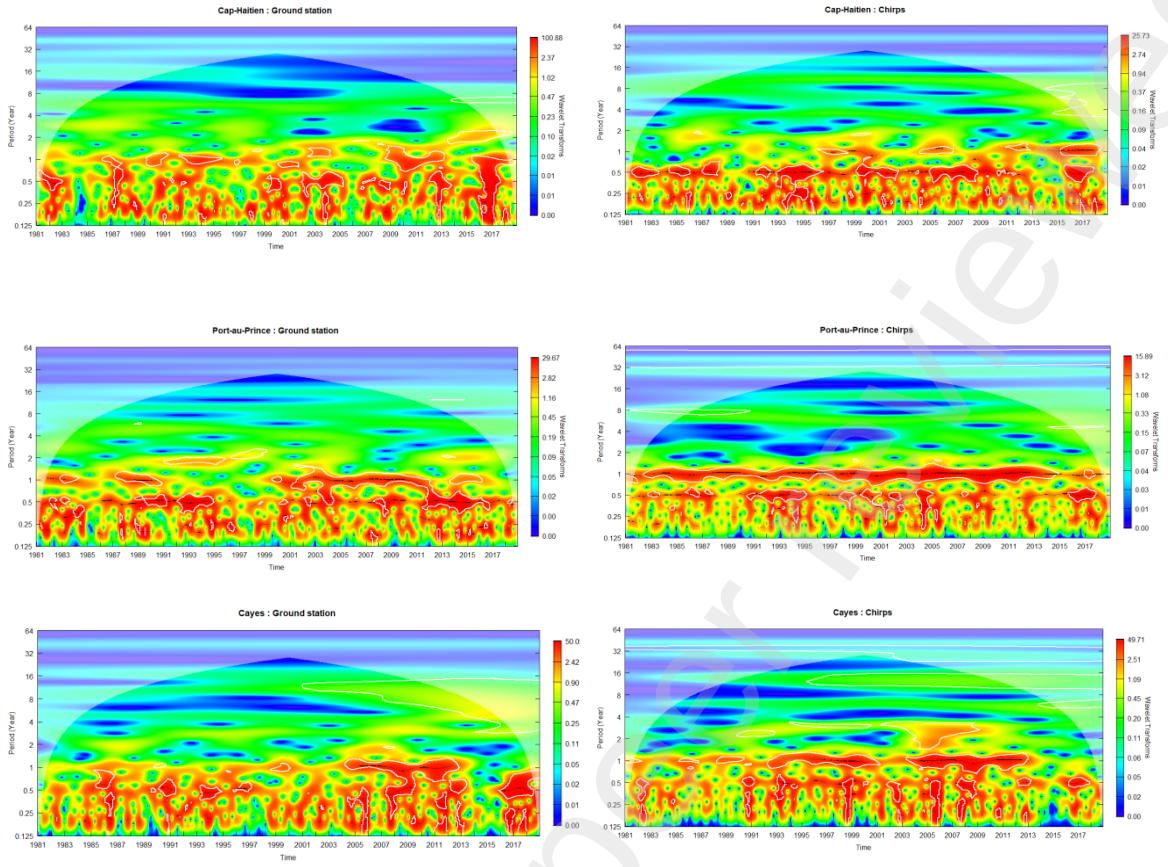

Preprint not peer reviewed

This preprint research paper has not been peer reviewed. Electronic copy available at: https://ssrn.com/abstract=5243924

Figure 7

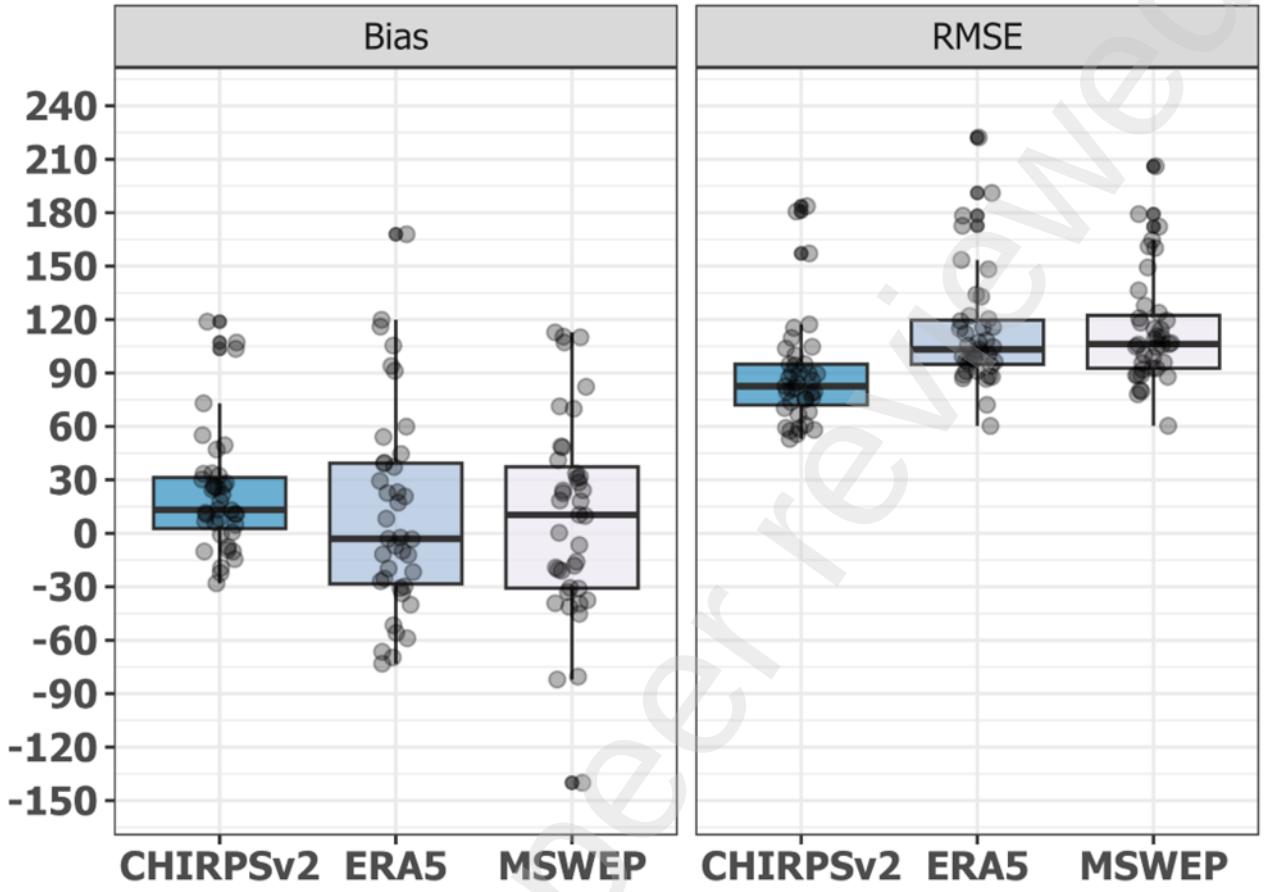

Preprint not peer reviewed

This preprint research paper has not been peer reviewed. Electronic copy available at: https://ssrn.com/abstract=5243924

Figure 8

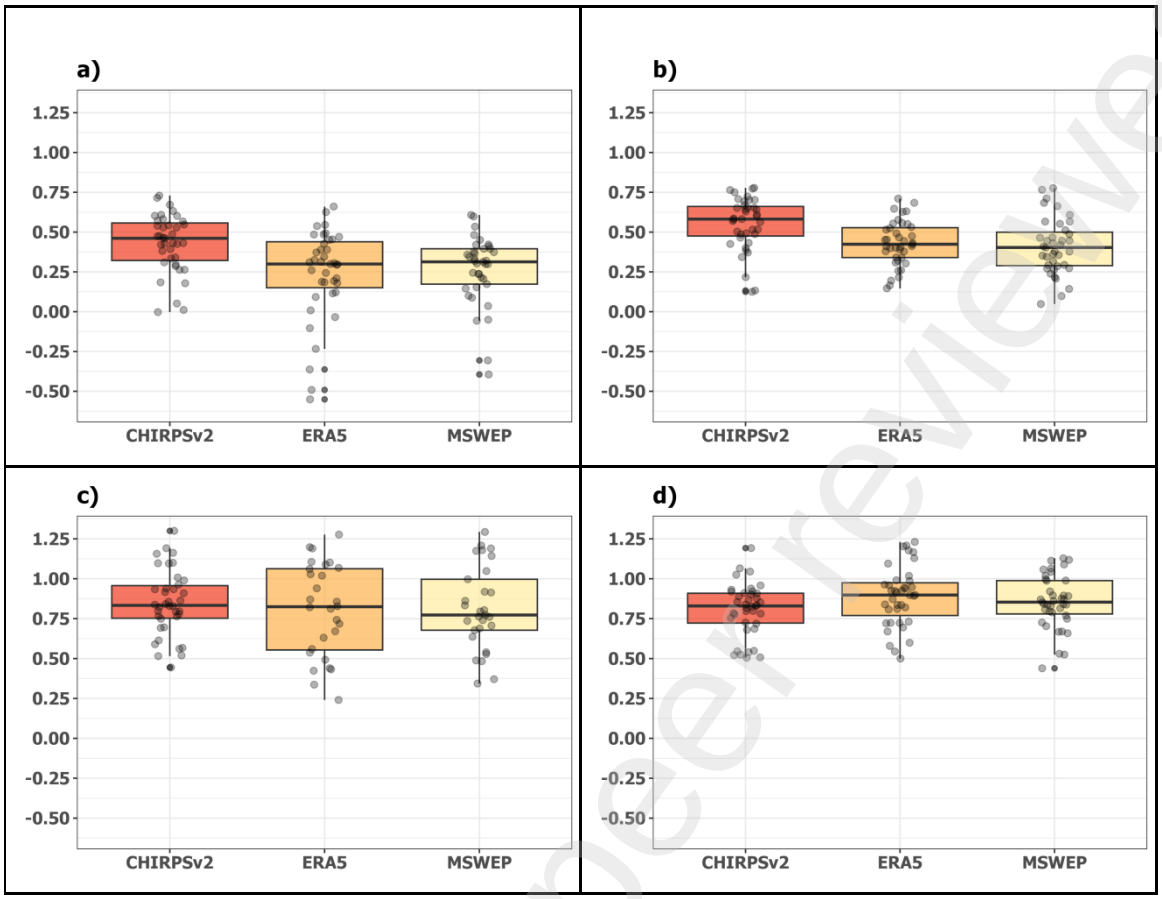

Preprint not peer reviewed

This preprint research paper has not been peer reviewed. Electronic copy available at: https://ssrn.com/abstract=5243924

Figure 9

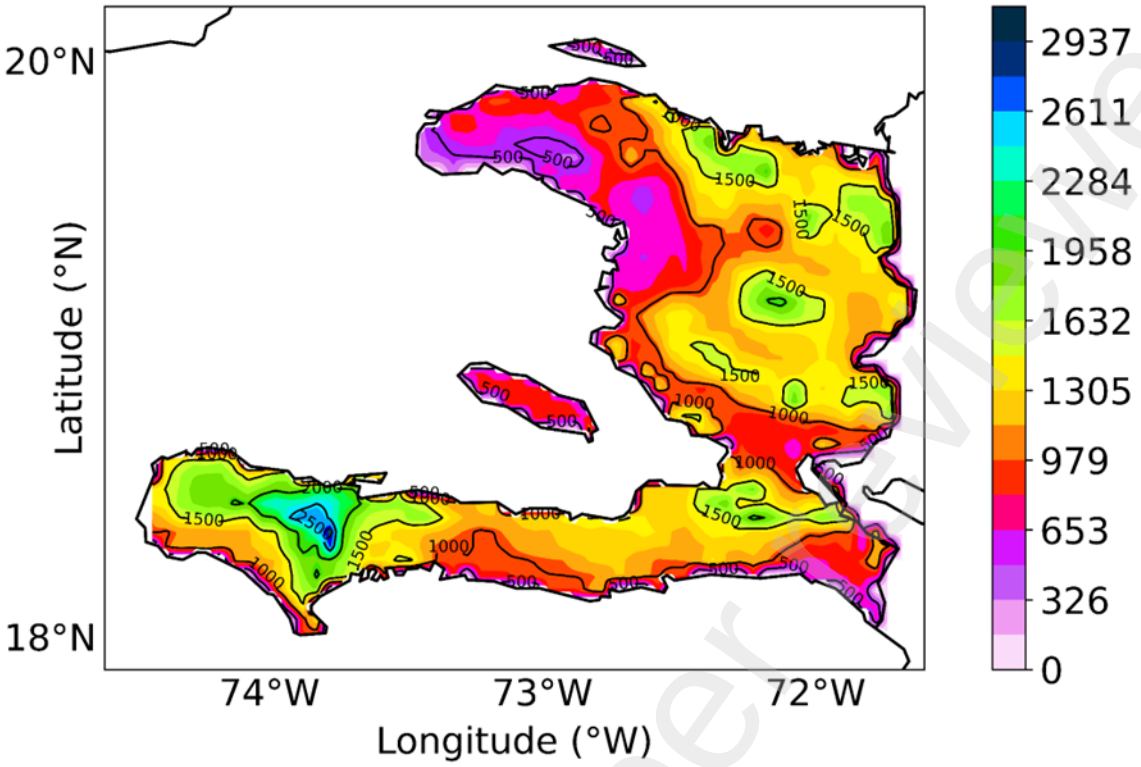

Preprint not peer reviewed

This preprint research paper has not been peer reviewed. Electronic copy available at: https://ssrn.com/abstract=5243924

Figure 10

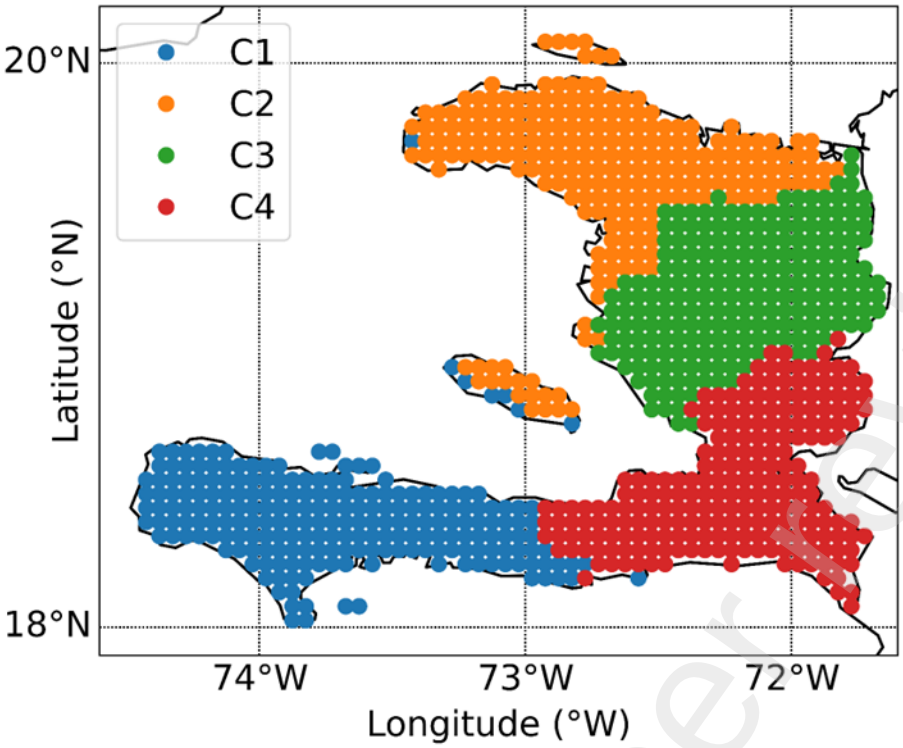

Preprint not peer reviewed

This preprint research paper has not been peer reviewed. Electronic copy available at: https://ssrn.com/abstract=5243924

Figure 11

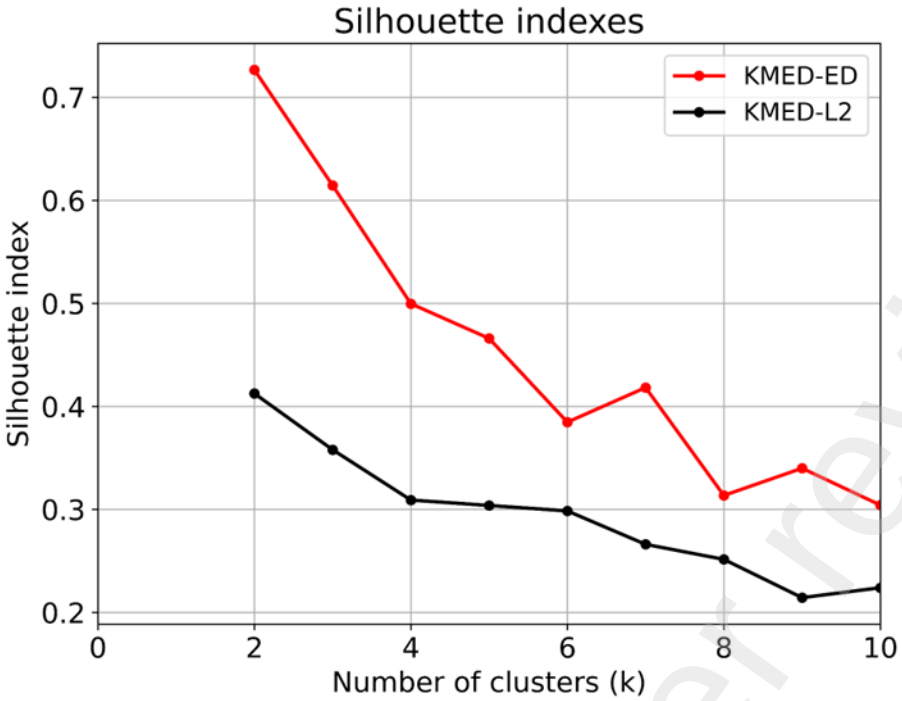

Preprint not peer reviewed

This preprint research paper has not been peer reviewed. Electronic copy available at: https://ssrn.com/abstract=5243924

Figure 12

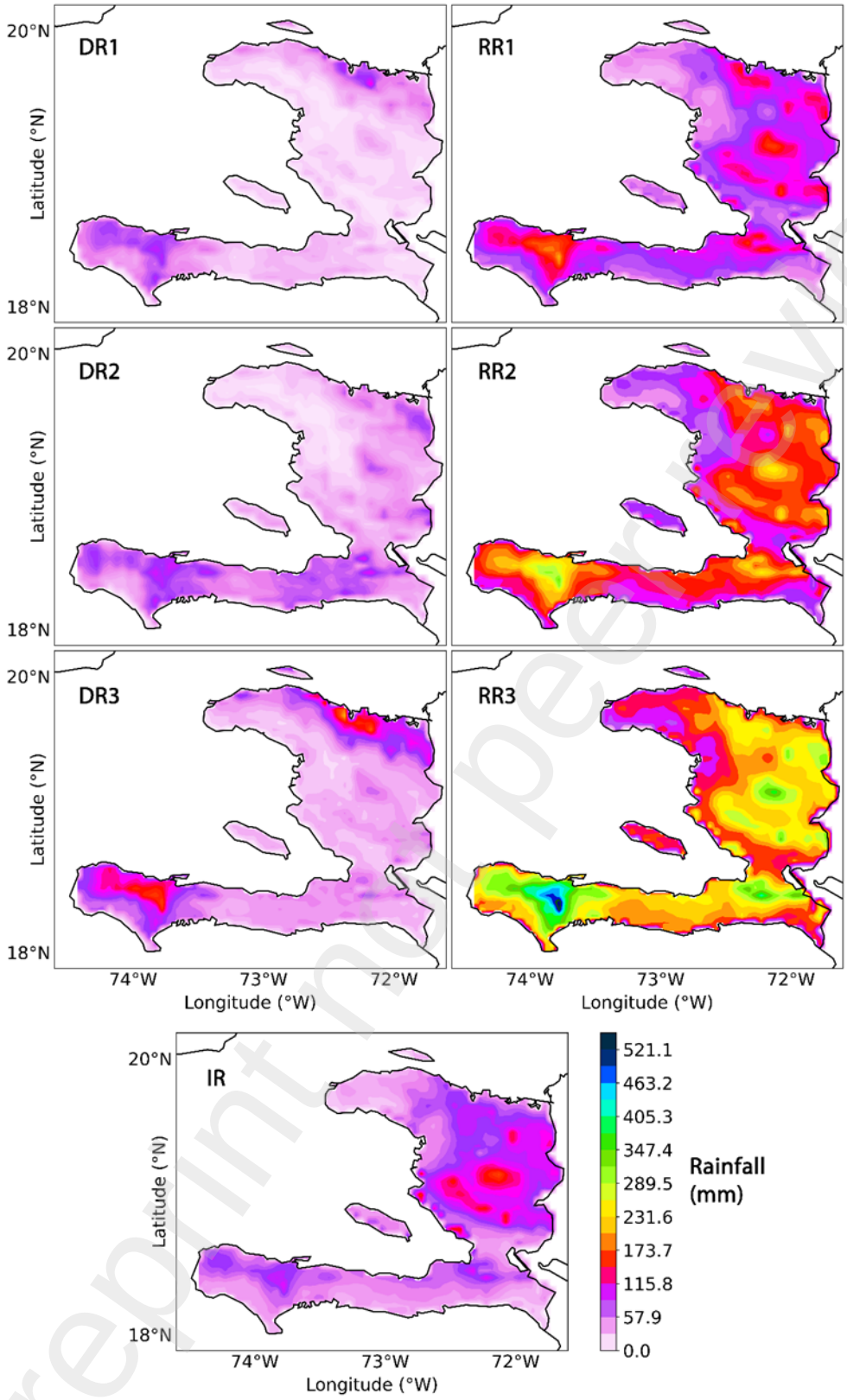

Preprint not peer reviewed

This preprint research paper has not been peer reviewed. Electronic copy available at: https://ssrn.com/abstract=5243924

Figure 13

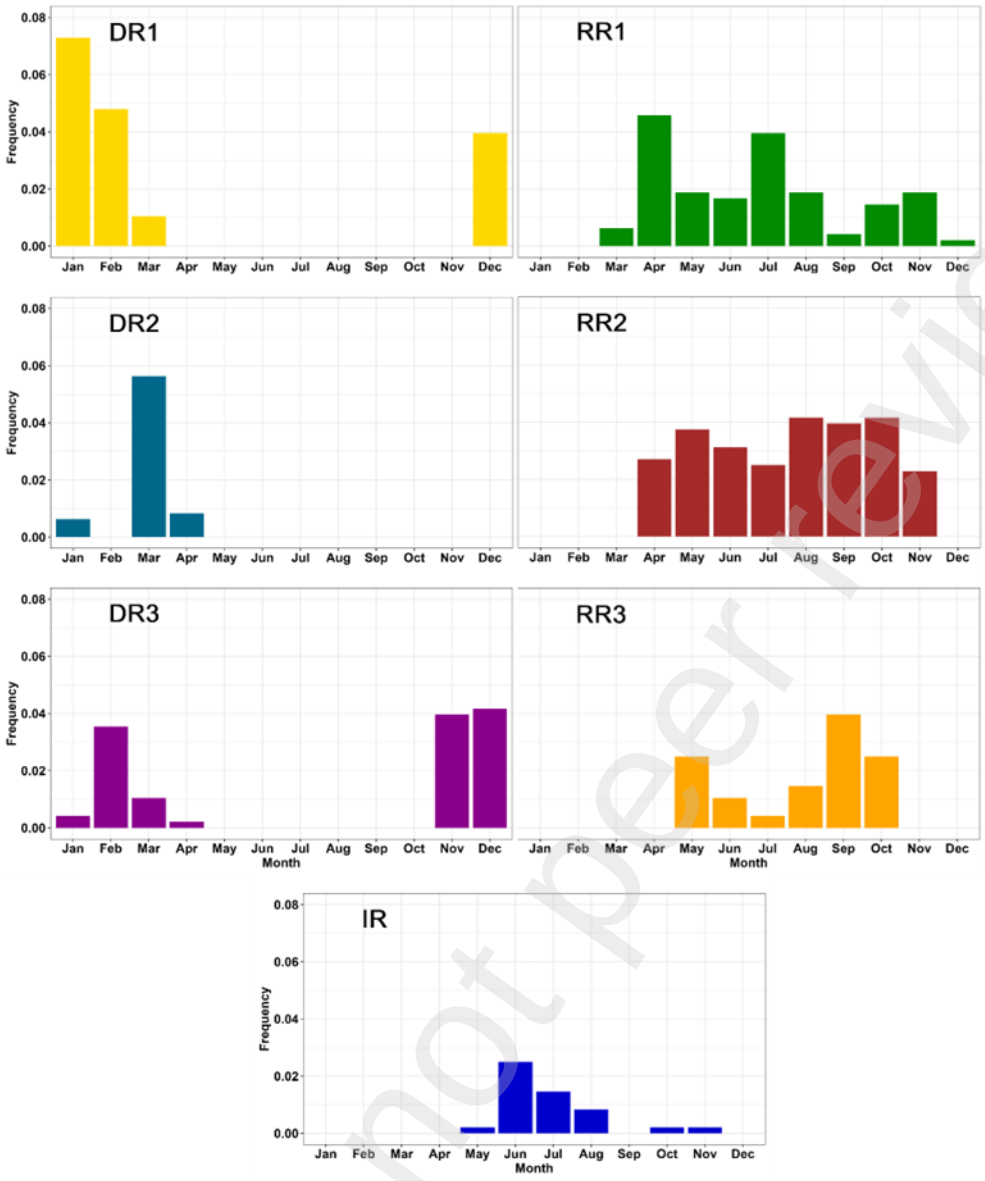

Preprint not peer reviewed

This preprint research paper has not been peer reviewed. Electronic copy available at: https://ssrn.com/abstract=5243924

Figure 14

	Years	Jan	Feb	Mar	Apr	May	Jun	Jul	Aug	Sep	Oct	Nov	Dec	Rainfall (mm)
Driest	2015	DR1	DR3	DR3	RR1	IR	IR	IR	RR1	RR2	RR3	RR2	DR3	902.5
	2013	DR1	DR1	DR2	DR2	RR1	IR	RR1	RR2	RR3	RR2	RR1	DR1	942.3
	2014	DR1	DR3	DR2	RR1	RR1	IR	RR1	RR2	RR2	RR1	RR1	DR3	945.4
	1989	DR1	DR3	DR2	DR2	RR2	IR	RR1	RR2	RR2	RR1	DR3	DR3	966.6
	2019	DR1	DR1	DR2	RR1	RR1	IR	RR1	IR	RR3	RR2	DR3	DR3	975.3
Others	1991	DR1	DR1	DR2	RR1	RR2	IR	IR	IR	RR2	RR1	RR2	DR1	981.3
	1982	DR2	DR1	DR1	RR1	RR3	IR	RR1	RR1	RR2	RR2	DR3	DR1	1020.7
	2018	DR3	DR3	DR3	RR1	RR2	RR1	IR	RR1	RR2	RR2	DR3	DR1	1030.8
	1986	DR1	DR1	DR2	RR2	RR2	RR2	RR1	RR1	RR1	RR2	DR3	DR1	1037.8
	2000	DR1	DR3	DR1	RR1	RR2	RR1	RR1	RR2	RR3	RR2	DR3	DR3	1042.6
	1983	DR1	DR1	RR1	RR1	RR2	RR2	RR1	RR1	RR2	RR3	DR3	DR1	1098.1
	1988	DR1	DR3	DR2	DR2	RR2	RR2	RR2	RR2	RR3	RR1	DR3	DR1	1112.4
	1992	DR1	DR3	DR2	RR1	RR3	IR	RR1	RR2	RR2	RR1	DR3	DR3	1137.0
	1997	DR1	DR3	DR2	RR1	RR1	RR2	RR1	RR2	RR3	RR3	RR1	DR1	1146.8
	1984	DR1	DR3	DR3	RR1	RR1	RR3	RR1	IR	RR3	RR2	DR3	DR1	1147.8
	2020	DR1	DR1	DR2	DR2	RR1	RR1	RR2	RR2	RR3	RR2	RR2	DR1	1154.4
	1981	DR2	DR3	DR2	DR3	RR2	RR2	RR2	RR2	RR2	RR2	RR1	DR3	1159.8
	2002	DR1	DR1	DR2	RR2	RR2	RR1	IR	RR2	RR3	IR	DR3	DR1	1162.9
	1985	DR1	DR1	DR2	RR1	RR2	IR	RR1	RR2	RR2	RR3	RR1	DR1	1186.6
	2009	DR1	DR1	DR2	RR1	RR3	RR3	RR1	RR2	RR2	RR1	DR3	DR3	1190.4
	1987	DR1	DR1	DR2	RR2	RR2	RR2	IR	RR1	RR2	RR2	RR1	RR1	1194.5
	2003	DR1	DR1	DR1	RR2	RR1	RR2	RR1	RR3	RR1	RR3	DR3	DR3	1196.2
	1990	DR1	DR1	DR2	RR1	RR1	RR2	RR1	RR1	RR3	RR3	RR1	DR1	1198.7
	2006	DR2	DR1	DR2	RR1	RR2	RR2	RR2	RR3	RR2	RR2	RR2	DR1	1207.5
	2004	DR1	DR3	DR2	RR1	RR3	IR	RR2	RR2	RR3	RR2	DR3	DR3	1225.2
	2001	DR1	DR1	DR2	RR1	RR3	IR	RR2	IR	RR3	RR2	RR1	DR3	1232.2
	1995	DR1	DR3	DR3	RR1	RR3	RR1	RR2	RR2	RR3	RR2	DR3	DR3	1256.0
	2012	DR1	DR1	DR2	RR2	RR2	RR1	IR	RR3	RR2	RR3	DR3	DR1	1267.8
	2016	DR1	DR1	DR2	RR2	RR3	RR1	RR1	RR1	RR2	RR3	RR1	DR3	1285.5
	2011	DR1	DR1	DR2	RR1	RR2	RR3	RR2	RR3	RR2	RR2	DR3	DR1	1305.1
	1994	DR1	DR3	DR2	RR2	RR3	IR	IR	RR2	RR2	RR2	RR2	DR3	1306.3
	1996	DR1	DR3	DR2	RR2	RR2	RR2	RR2	RR2	RR2	RR3	RR2	DR3	1345.4
	1999	DR1	DR3	DR2	RR1	RR1	RR2	RR1	RR2	RR3	RR3	RR2	DR3	1378.9
	2008	DR1	DR1	DR1	RR2	RR2	RR2	RR1	RR3	RR3	RR2	DR3	DR1	1391.2
	1998	DR1	DR3	RR1	RR1	RR2	RR2	RR2	RR3	RR3	RR2	DR3	DR3	1395.2
Rainiest	1993	DR3	DR1	DR2	RR2	RR3	RR2	RR1	RR1	RR3	RR1	RR2	DR3	1439.5
	2017	DR1	DR1	DR3	RR2	RR3	RR2	RR2	RR2	RR3	RR2	RR2	DR1	1462.4
	2007	DR1	DR1	RR1	RR2	RR3	RR1	RR2	RR2	RR2	RR3	RR2	DR3	1474.8
	2010	DR1	DR3	DR2	RR2	RR2	RR3	RR3	RR2	RR3	RR2	RR2	DR3	1529.6
	2005	DR1	DR1	DR1	RR1	RR3	RR3	RR3	RR3	RR3	RR3	IR	DR1	1693.2

Preprint not peer reviewed

This preprint research paper has not been peer reviewed. Electronic copy available at: https://ssrn.com/abstract=5243924

Figure 15

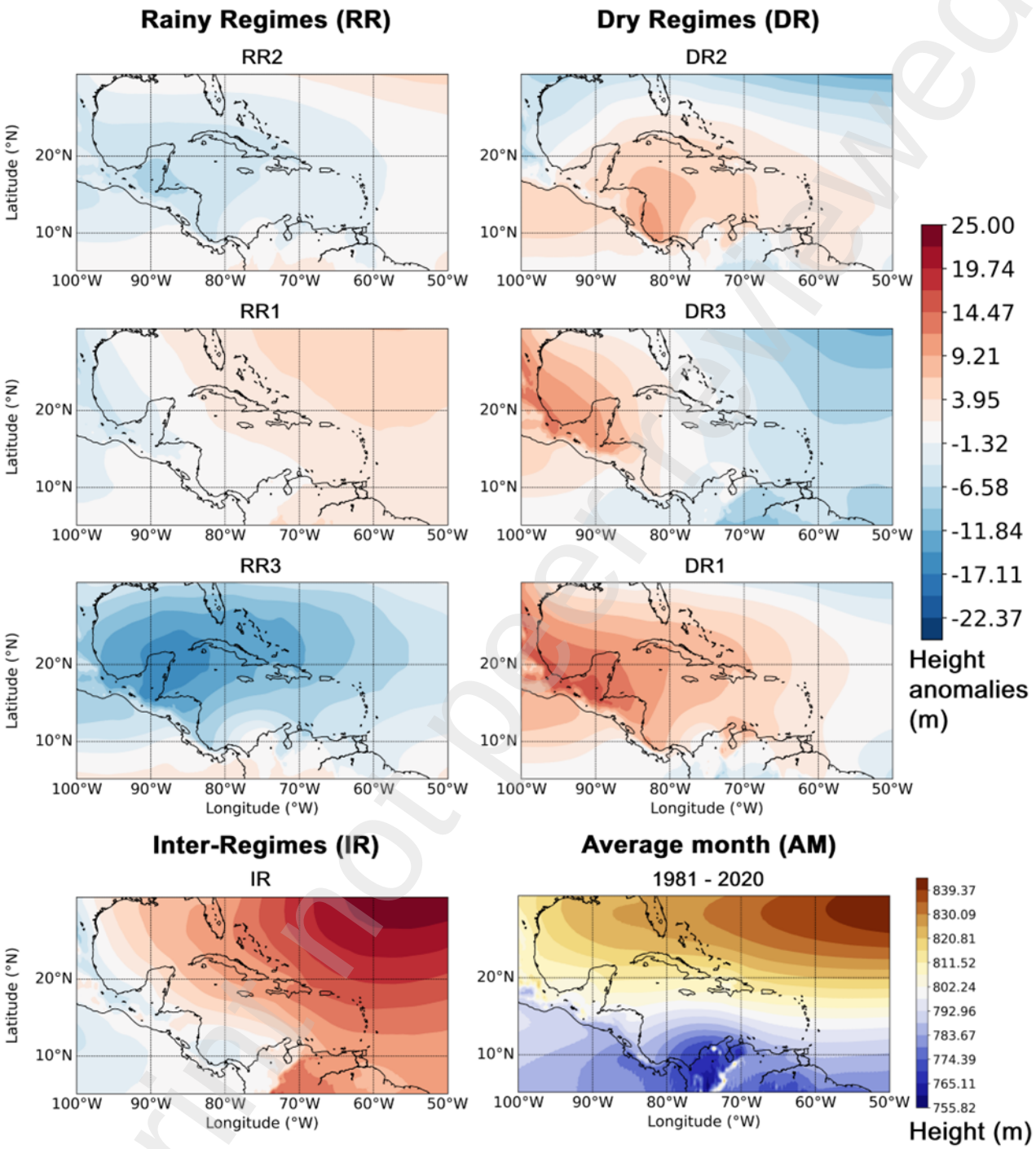

Preprint not peer reviewed

This preprint research paper has not been peer reviewed. Electronic copy available at: https://ssrn.com/abstract=5243924

Figure 16

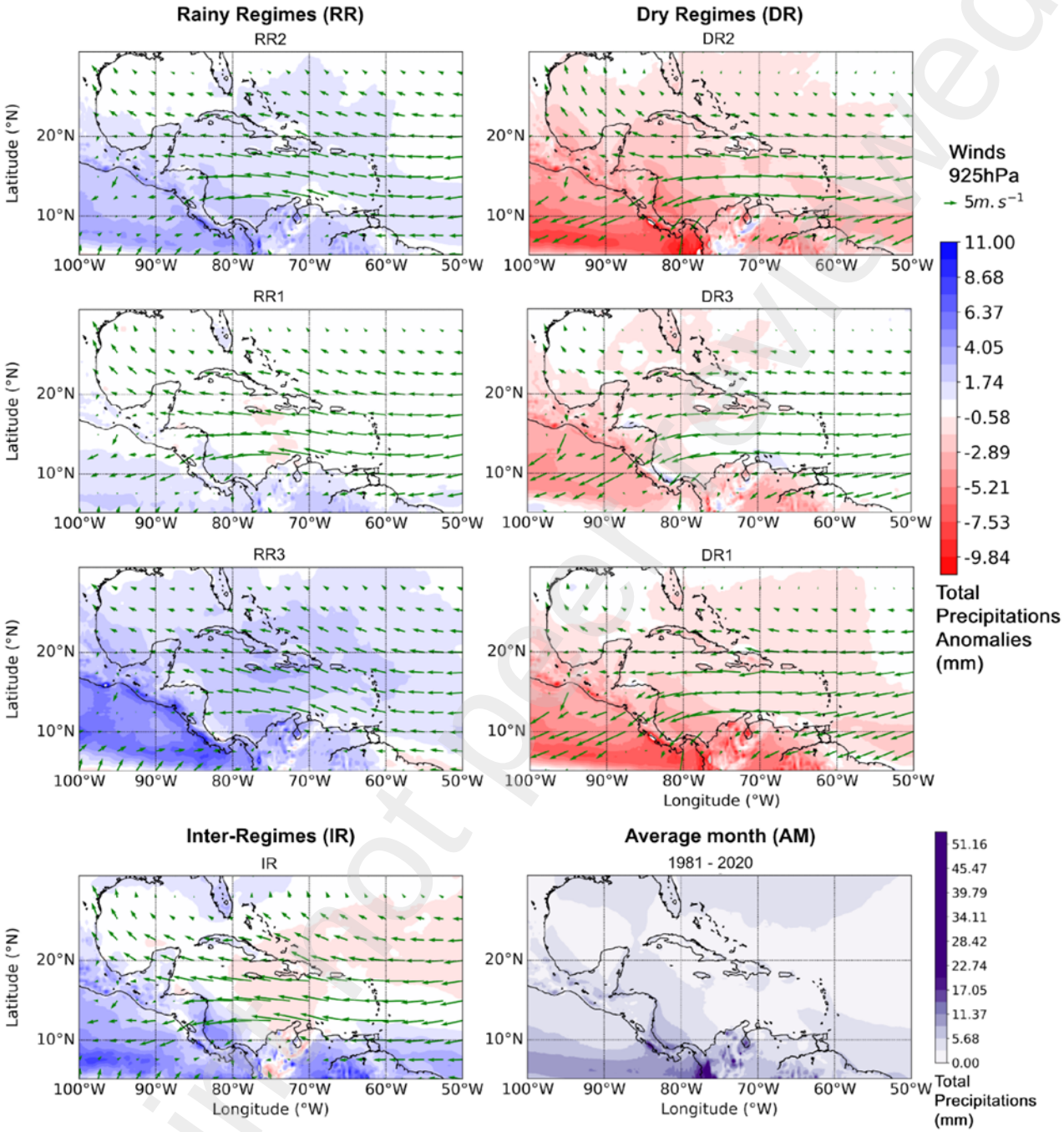

Preprint not peer reviewed

This preprint research paper has not been peer reviewed. Electronic copy available at: https://ssrn.com/abstract=5243924

Figure 17

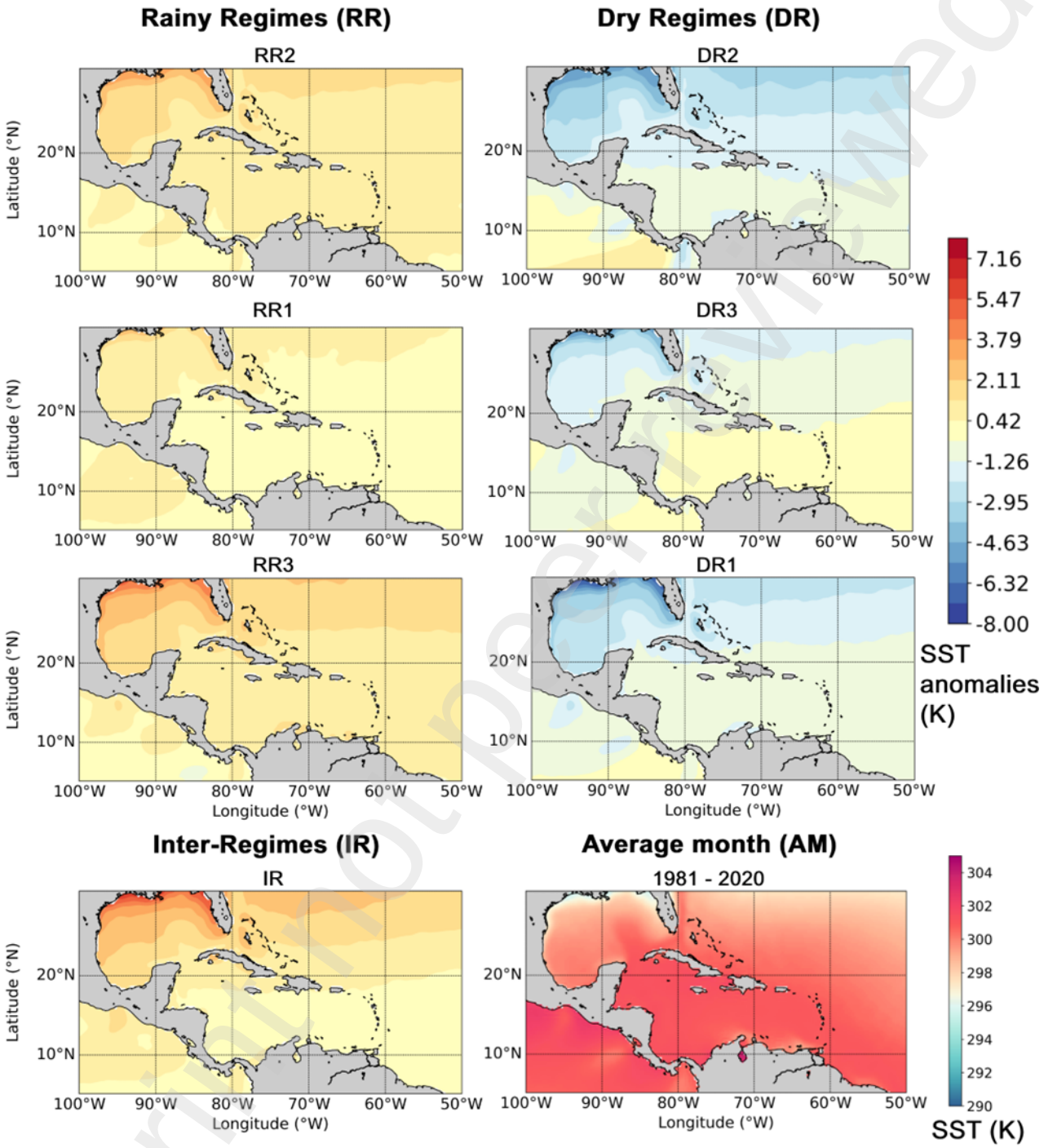

Preprint not peer reviewed

This preprint research paper has not been peer reviewed. Electronic copy available at: https://ssrn.com/abstract=5243924

Figure 18

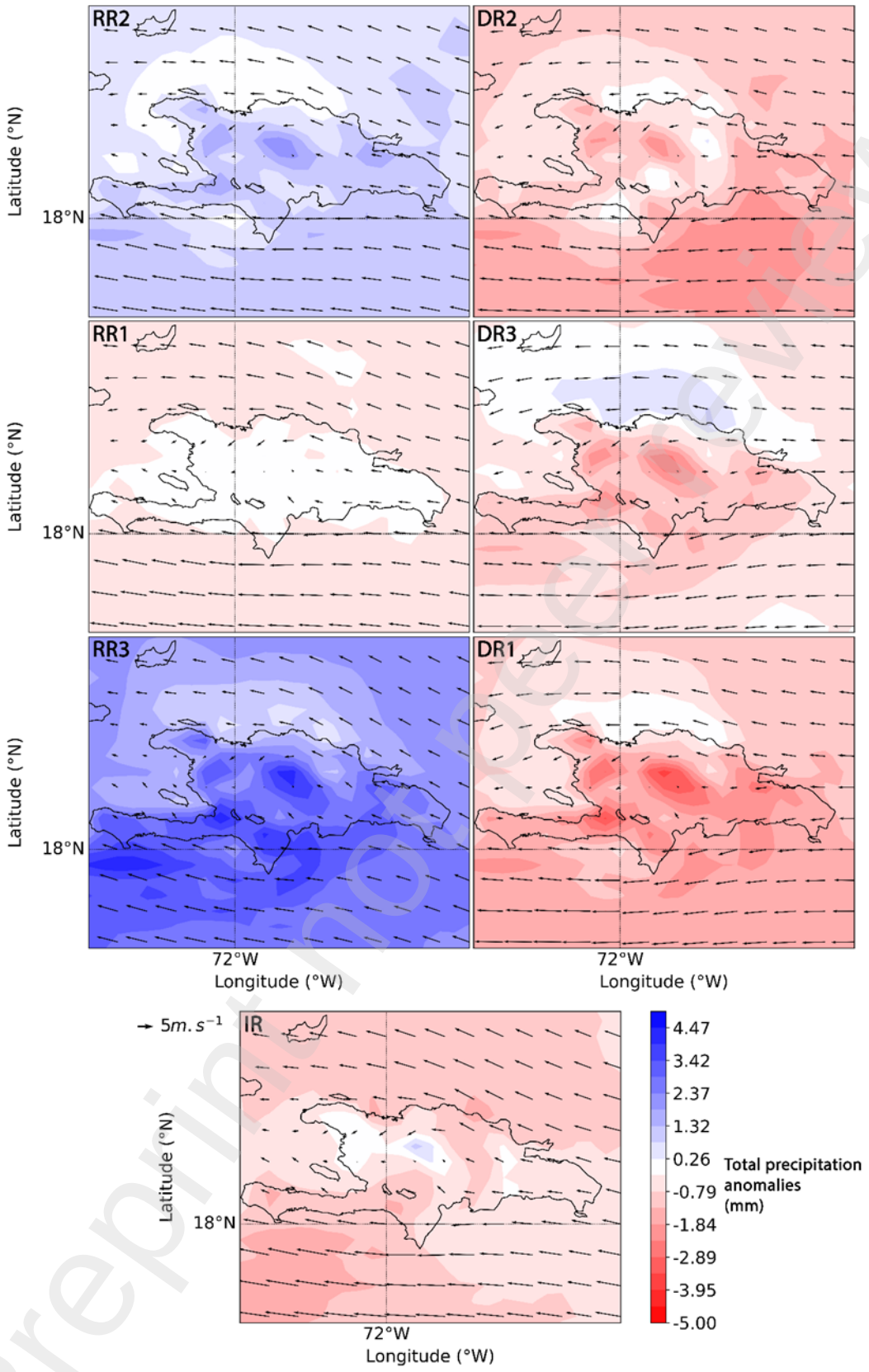

Preprint not peer reviewed

This preprint research paper has not been peer reviewed. Electronic copy available at: https://ssrn.com/abstract=5243924